Proximate Time-Optimal Control of a Harmonic Oscillator

Roger A. Braker and Lucy Y. Pao

***Abstract*—This paper considers near time-optimal setpoint tracking of a second-order oscillator. First, the time-optimal setpoint tracking feedback law is derived by recasting the problem as a regulator problem in the error coordinates with shifted control limits. This result is used to construct a de-rated approximation of the optimal control. Initially, the control law is derived as a regulator controller. This result is then extended to include setpoint tracking. Global stability is proven for the setpoint tracking controller in the zero-damping case. A scaling method is developed which allows an efficient implementation of the control laws using a single look-up table. Both the damped and un-damped controllers are validated experimentally.**

***Index Terms*—Flexible structures, proximate time-optimal control.**

I. INTRODUCTION

In this paper, we are concerned with the near minimum-time setpoint tracking of systems which can be described as a damped harmonic oscillator

$$G(s) = \frac{b_1 s + b_o}{s^2 + 2\zeta\omega s + \omega^2} \tag{1}$$

when the input is subject to saturation. Such systems arise in various applications ranging from DC-DC buck converters [1], the x-y micro-positioners used in scanning probe microscope-based data storage systems [2]–[4], to power networks [5]. Fast setpoint tracking is also of interest in certain Atomic Force Microscopy (AFM) imaging methods [6], [7]. The piezo-electric stage of some AFMs can also be adequately described by a damped harmonic oscillator [8, p.179].

For a linear time-invariant system, Pontryagin's Minimum Principle leads to a time-optimal control that is bang-bang [9]. For low-order systems, the bang-bang control can be expressed by a feedback control law, characterized by a switching surface. Excellent resources for synthesizing these feedback laws can be found in [10]–[12]. Unfortunately, the bang-bang feedback control is impractical. In any real control system, there will be process and measurement noise, uncertainty in the system parameters, and finite actuation bandwidth which will cause the control to chatter between its maximum and minimum values, which is undesirable in many systems. It has furthermore been shown that for some plants, a bang-bang feedback control can lead to a limit cycle for arbitrarily small variations in plant parameters [13].

A large body of work exists which develops methods to combat these problems. Reference [14] suggests pre-computing the time-optimal trajectory which is then tracked with a stabilizing trajectory tracking control law. At the end of this reference trajectory, an end-game control law is implemented to eliminate any final error. Although such an approach is applicable to higher-order systems, a downside to this method is it requires pre-computation of individual trajectories for each initial condition and target state.

Reference [15] shows that, within a certain subset of the state space, the non-linear switching surface can be replaced with a linear plane which intersects the switching surface at the switch points. They then show how to effectively approximate the optimal control with a high-gain linear feedback. The downside to this method is, again, that the intersecting plane changes for each initial condition and target point.

The Proximate Time-Optimal Servomechanism (PTOS) is one of the most popular techniques in robust time-optimal control. However, the theory has been developed largely with a focus on rigid-body systems. The PTOS was first developed by Workman [16]–[18] for the double integrator plant, and later extended to a triple integrator plant [19]. Numerous other extensions and improvements have been developed over the years. Constant closed-loop damping of the PTOS was achieved in [20] by scheduling the velocity gain as a function of position error, yielding faster settling time than traditional PTOS. In [21], [22], the linear region of PTOS is replaced with a non-linear function enabling the elimination of the acceleration discount factor, which results in considerably faster settling time. The PTOS has been extended to include friction [23] and high frequency flexible modes [24]. Recently, a two degree of freedom PTOS controller has been proposed, the MPTOS, which allows additional flexibility in the design [25].

Two exceptions to the focus on rigid bodies are [2] and [3]. These works propose PTOS controllers for an x-y micro-scanner modeled as (1). However, both approximate the true oscillator switching curve with the switching curve for a rigid body plant. As they note, this approximation is only valid for a limited range of model parameters and a limited subset of the phase space.

Our earlier work in developing a PTOS-like controller for systems which can be described by (1) are [26] and [27]. In [26], we developed a near time-optimal controller, PTOSω, for (1) when $\zeta = 0$ and proved global stability. This controller is only applicable to regulation to the origin. In [27],

The authors are with the Dept. of Electrical, Computer, and Energy Engineering at the University of Colorado, 425 UCB, Boulder, CO 80309, United States. Phone: +1 (303) 492-2360. Fax: +1 (303) 492-2758. R. A. Braker (corresponding author roger.braker@colorado.edu) is a graduate student and L.Y. Pao (pao@colorado.edu) is the Richard & Joy Dorf Professor.

This work was supported in part by the US National Science Foundation (NSF Grant CMMI-1234980), Agilent Technologies, Inc., and the Hanse Wissenschaftskolleg in Delmenhorst, Germany.

we outlined how to extend the PTOSω regulator to include setpoint tracking, also for the case $\zeta = 0$. The controller did not include the so-called "acceleration discount factor" α, and stability was not proved. The main contributions of this work, relative to [26] and [27], are to:

1) Derive PTOS-like controllers, PTOSω ($\zeta = 0$) and PTOS$\omega\zeta$ ($\zeta \in (0,1)$) setpoint tracking controllers under a common framework, which are based on the true time-optimal switching curve for the subset of the state-space which is of interest for setpoint tracking applications – outside this region, the controllers use a sub-optimal approximation to ensure the control is well defined globally. In contrast to [27], this controller includes the acceleration discount factor and also addresses the damped case.
2) Prove global stability of the PTOSω (i.e., $\zeta = 0$) setpoint tracking controller, again in contrast to [27].

We do not prove stability for the case when $\zeta \in (0,1)$. As more minor contributions relative to [26] and [27], we give a discussion of design considerations and also develop a scaling method that permits an efficient implementation of either control law using a single look-up table. Both controllers are validated experimentally.

This paper is organized as follows. Section II formulates the basic problem setting and reviews the synthesis of the time-optimal feedback control law for the general case of setpoint tracking. By considering the error coordinates, we recast setpoint tracking as a regulation problem with shifted control limits. We show that these shifted control limits imply an asymmetric switching curve, in contrast to both rigid-body time-optimal control as well as the more commonly derived minimum-time regulation problem for the harmonic oscillator. In Section III, we derive the special case of the PTOSω and PTOS$\omega\zeta$ regulator. With this insight, we then extend the regulator to include setpoint tracking in Section IV. In Sections V and VI, we specialize the development to the case $\zeta = 0$, proving global stability of PTOSω in Section V and exploring design implications in Section VI.

In Section VII, we show how either controller can be efficiently implemented using a look-up table combined with a scaling technique to account for the reference dependent switching curve. In Section VIII, we show experimental results for the setpoint tracking PTOSω and PTOS$\omega\zeta$, which includes a demonstration of the scaling method. We also compare the PTOSω to the near time-optimal control method developed in [15]. Finally, we provide concluding remarks in Section IX.

II. PROBLEM FORMULATION

The damped oscillator, (1), can be represented in state space as

$$\begin{aligned} \dot{x} &= Ax + Bu \\ y &= Cx, \end{aligned} \tag{2}$$

where

$$A = \begin{bmatrix} 0 & 1 \\ -\omega^2 & -2\zeta\omega \end{bmatrix}, \quad B = \begin{bmatrix} 0 \\ b_o \end{bmatrix}, \quad C = \begin{bmatrix} 1 & b_1/b_o \end{bmatrix}. \tag{3}$$

We assume throughout this paper that $0 \le \zeta < 1$ so that the imaginary part of the eigenvalues of A are non-zero. As a matter of convenience, we will colloquially refer to x_1 and x_2 as "position" and "velocity", which is only technically correct if $b_1 = 0$. This should not cause confusion because we will not reference $y(t)$ or C for the rest of the paper.

Equation (2) is solved by the variation of constants formula

$$x = e^{A(t)}x_o + \int_0^t e^{A(t-\tau)}Bu(\tau)d\tau \tag{4}$$

where $x_o = x(0)$ and the state transition matrix is given by

$$e^{At} = e^{-t\sigma}\begin{bmatrix} \cos(\omega_d t) + \frac{\zeta \sin\omega_d t}{\sqrt{1-\zeta^2}} & \frac{\sin(\omega_d t)}{\omega_d} \\ -\frac{\omega\sin(\omega_d t)}{\sqrt{1-\zeta^2}} & \cos(\omega_d t) - \frac{\zeta\sin\omega_d t}{\sqrt{1-\zeta^2}} \end{bmatrix} \tag{5}$$

where $\sigma = \zeta\omega$ and $\omega_d = \omega\sqrt{1-\zeta^2}$. For the minimum-time problem to make sense, we must assume a bounded control input. In particular, we assume that the system has symmetric control limits such that $u(t) \in [-u^+, +u^+]$, for $u^+ > 0$.

In this paper, we will draw a distinction between *regulation* and *setpoint tracking*. By regulation, we mean driving some initial condition to the origin of the state space and holding it there. By setpoint tracking, we mean driving some initial condition to a holdable equilibrium,

$$\mathcal{H}_{eq} = \left\{x : x = -A^{-1}Bu,\, u \in [-u^+,\, +u^+]\right\}, \tag{6}$$

and holding it there. For the state space representation in (3), $\mathcal{H}_{eq}$ is a line segment in $\mathbb{R}^2$ on the x_1-axis between $[-cu^+, +cu^+]$ where $c = \frac{b_o}{\omega^2}$. Although regulation is certainly a subset of setpoint tracking, we draw this distinction since, as we will see, regulation has a convenient symmetry lacking in the setpoint tracking problem. More formally, we can state our objectives as:

Problem 1: (Minimum-Time Regulation) Given the system (2)-(3) and any initial state $x(0) = x_o$, transfer the system to the origin of the state space in minimum time t_f and hold it there $\forall\ t \ge t_f$.

Problem 2: (Minimum-Time Setpoint Tracking) Given the system (2)-(3) and any initial state $x(0) = x_o$, transfer the system to a setpoint, $x_r \in \mathcal{H}_{eq}$, in minimum time t_f and hold it there $\forall\ t \ge t_f$.

A. Review of the Time-Optimal Feedback Control

The time-optimal solutions to Problems 1-2 can be derived from Pontryagin's Minimum Principle. In standard texts, this is typically done for *Problem 1*, the regulator case [9]–[12]. The setpoint tracking case has also been derived previously [28], [29], which we briefly review here with minor adjustments.

Let $x_r = [x_{1r}\ 0]^T \in \mathcal{H}_{eq}$ be the desired setpoint which in steady state requires a feedforward control $u_{ss} = x_{1r}/c$. We recast setpoint tracking as a regulation problem by considering the error coordinates, $x_e = x - x_r$. The error dynamics are described by

$$\begin{aligned} \dot{x}_e &= Ax_e + Ax_r + Bu \\ &= Ax_e + \begin{bmatrix} 0 \\ b_o \end{bmatrix}\bar{u}(t), \end{aligned} \tag{7}$$

where $\bar{u}(t) = u - \frac{1}{c}x_{1r}$. Thus, driving the system to $x(t_f) = x_r$ is equivalent to driving the error state x_e to the origin if the error dynamics are driven by a control, $\bar{u}(t)$, with asymmetric saturation, namely

$$\bar{u}^+ = u^+ - \frac{1}{c}x_{1r} \tag{8}$$

$$\bar{u}^- = -u^+ - \frac{1}{c}x_{1r}. \tag{9}$$

To avoid duplicating equations that only differ by changing $\bar{u}^+$ to $\bar{u}^-$, we will refer to (9) and (8) together by the placeholder $\bar{u}^\pm := \pm u^+ - \frac{1}{c}x_{1r}$. Since we assume that $x_r \in \mathcal{H}_{eq}$, we can parameterize $\bar{u}^\pm$ as

$$\bar{u}^+ = u^+(1-\gamma) \tag{10}$$

$$\bar{u}^- = u^+(-1-\gamma) \tag{11}$$

where

$$\gamma = \frac{x_{1r}}{u^+ c} \in (-1,\, 1).$$

Thus the optimization problem to solve for Problems 1 and 2 is

$$\begin{aligned} \min \int_0^{t_f} 1 \cdot d\tau \\ \text{s.t. } \dot{x}_e(t) = Ax_e(t) + B\bar{u}(t), \\ x_e(0) = x_o - x_r,\ x_e(t_f) = 0 \\ \bar{u} \in [\bar{u}^-,\, \bar{u}^+]. \end{aligned} \tag{12}$$

The Hamiltonian for this problem is

$$H(x_e, \bar{u}, p) = 1 + p(t)^T \left(Ax_e(t) + B\bar{u}(t)\right). \tag{13}$$

Solving the two-point boundary-value problem

$$\begin{aligned} \dot{x}_e(t) &= H_p = Ax_e(t) + B\bar{u}(t) \\ -\dot{p}(t) &= H_{x_e}^T = A^T p(t) \\ \bar{u}(t) &= \arg \min_{\bar{u} \in [\bar{u}^-,\, \bar{u}^+]} H\left(x_e(t), \bar{u}(t), p(t)\right) \\ \text{s.t.} \quad & x_e(0) = x_0 - x_r,\ x_e(t_f) = 0, H(t) = 0, \end{aligned} \tag{14}$$

yields the time-optimal control, and various methods exist to compute $\bar{u}(t)$ as an open-loop control. For our purpose however, we would prefer the optimal control as a feedback law. Because $\bar{u}(t) \in [\bar{u}^-, \bar{u}^+]$ is bounded, the optimal control is

$$\bar{u} = -\mathrm{sgn}_a(p(t)^T B) = -\mathrm{sgn}_a(p_2(t) b_o) \tag{15}$$

where we define the asymmetric signum function as

$$\mathrm{sgn}_a(\xi) := \begin{cases} \bar{u}^+, & \xi > 0 \\ 0, & \xi = 0 \\ \bar{u}^-, & \xi < 0. \end{cases} \tag{16}$$

Thus, the control switches when the costate velocity, $p_2(t)$, vanishes. The condition $H(t) = 0$ guarantees $p(t) \neq 0$ while the additional fact that the system is controllable guarantees that $p^T(t)B = 0$ at only a finite number of points [30, ch. 5]. It follows that given (5) and (14), the costate velocity can be expressed as $p_2(t) = \beta e^{\sigma t} \sin(-\omega_d t + \phi)$, where the constants $\beta \neq 0$ and ϕ depend on the initial condition of the costate. This implies that the control is never constant for longer than π/ω_d units of time. Hence, we can locate the final leg of any time-optimal trajectory by solving (7) backwards in time from the origin of the error phase plane for half a period with $\bar{u}(t)$ alternately fixed at $\bar{u} = \bar{u}^+$ and $\bar{u} = \bar{u}^-$ which results in two curves, $\mathcal{S}_1^\pm$ (see Fig. 1). Because any time-optimal trajectory with an initial condition not on $\mathcal{S}_1^\pm$ must have switched at some point on $\mathcal{S}_1^\pm$, we can again integrate backwards for π/ω_d units of time from all points on $\mathcal{S}_1^\pm$ with $\bar{u} = \bar{u}^\mp$ to locate a new curve, $\mathcal{S}_2^\mp$. In other words, $\mathcal{S}_2^-$ is obtained by rotating $\mathcal{S}_1^+$ counter-clockwise by π radians about the point $(c\bar{u}^-,\, 0)$ and scaling it by $\exp(\frac{\sigma\pi}{\omega_d})$ [28]. Similarly, $\mathcal{S}_2^+$ is obtained by rotating $\mathcal{S}_1^-$ counter-clockwise by π radians about the point $(c\bar{u}^+,\, 0)$ and scaling it by $\exp(\frac{\sigma\pi}{\omega_d})$. Continuing this process generates the time-optimal *switching curve*, $\mathcal{S} = \cup_{i=1}^{\infty} \mathcal{S}_i^\pm$.

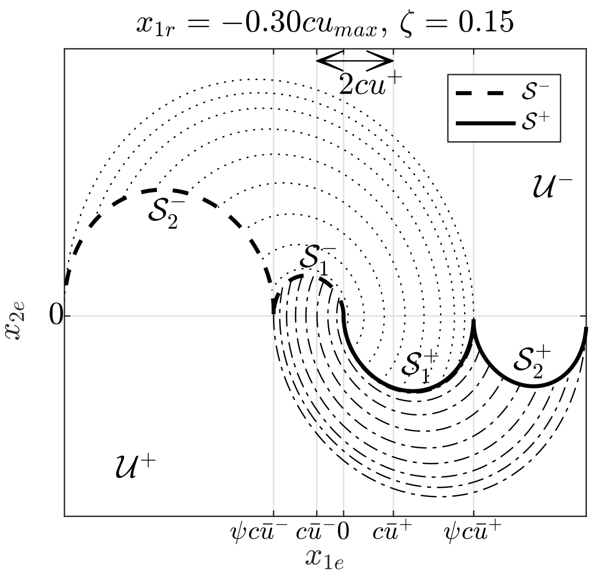

Fig. 1: Illustration of the generation of the time-optimal switching curve. The first dashed (resp., solid) curves, $\mathcal{S}_1^-$ (resp., $\mathcal{S}_1^+$), are generated by integrating backward from $(0,0)$ with $\bar{u}(t)$ held constant at $\bar{u}^-$ (resp., $\bar{u}^+$). The dotted curves represent integrating backward from all points on $\mathcal{S}_1^+$ with $\bar{u}(t) = \bar{u}^-$, while the dash-dotted curves are trajectories flowing backward from $\mathcal{S}_1^-$ with $\bar{u}(t) = \bar{u}^+$.

The first set of switching curves $\mathcal{S}_1 = \mathcal{S}_1^- \cup \mathcal{S}_1^+$ are obtained by performing the integration

$$x_e^*(t_o) = \bar{u}^\pm \int_{t_f}^{t_o} e^{A(t_o - \tau)} B d\tau \tag{17}$$

which yields

$$\begin{bmatrix} x_{1e}^*(t_o) \\ x_{2e}^*(t_o) \end{bmatrix} = \bar{u}^\pm e^{-\sigma(t_o - t_f)} \begin{bmatrix} -c & -\frac{b_o\zeta}{\omega_d\omega} \\ 0 & \frac{b_o}{\omega_d} \end{bmatrix} \begin{bmatrix} \cos\omega_d(t_o - t_f) \\ \sin\omega_d(t_o - t_f) \end{bmatrix} + \begin{bmatrix} c\bar{u}^\pm \\ 0 \end{bmatrix}. \tag{18}$$

The same result, less a translation of x_{1r}, will be obtained by generating the switching curve in the un-shifted coordinates by integrating (4) backwards from x_r with $u(t) = \pm u^+$.

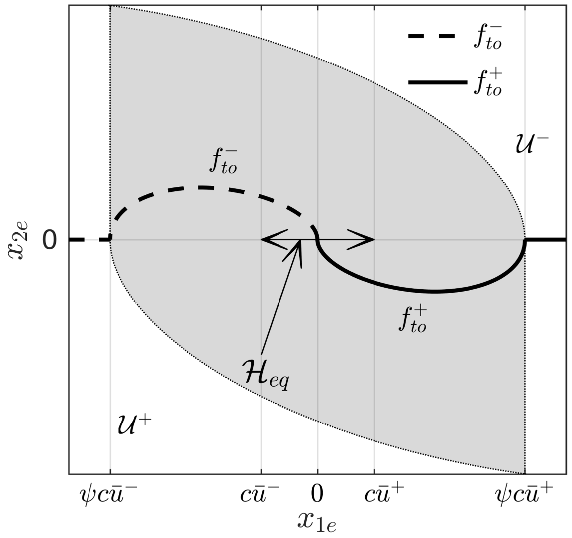

Fig. 2: For the regulator case ($\zeta = 0.3$), this figure depicts the sub-optimal flattening of the switching curve far from the origin. The gray shaded region is the region $\mathcal{Q}$ (defined in (21)), which we consider the typical operating region for setpoint tracking applications.

The parametric equation (18) describes a spiral (or ellipse when $\zeta = 0$) which rotates about the rotation center $c\bar{u}^{\pm}$. The x_{1e}-axis length of each curve is given by $\psi c\bar{u}^{\pm}$ where

$$\psi = 1 + e^{\sigma\pi/\omega_d}. \tag{19}$$

To ease notation, we shall assume that $t_f = 0$ in (18) and that $t_0 \in [-\pi/\omega_d, 0]$. Because $\dot{x}_{1e} = x_{2e}$, then we see from (18) the x_{1e}^* portion of the switching curve will be monotonic. Thus, to each $x_{1e}^*(t_i)$ there corresponds a unique $x_{2e}^*(t_i)$ so that the tuple (x_{1e}^*, x_{2e}^*) represents a function

$$x_{1e}^*(t_i) \mapsto f_{to}^{\pm}(x_{1e}^*(t_i)) = x_{2e}^*(t_i) \tag{20}$$

which is the switching curve. The notation f_{to}^+ (resp., f_{to}^-) indicates the function was generated with $\bar{u}^+$ (resp., $\bar{u}^-$) in (18). We use the convention that the superscript "$^-$" denotes switching curve segments of the left-half phase plane and "$^+$" for the right-half phase plane through the rest of this paper.

Although it is possible to extend these expressions for the rest of the switching curve, this quickly becomes cumbersome. Moreover, our primary interest here is in systems that move between setpoints. As seen in Fig. 2, the first set of switching curves, f_{to}^- and f_{to}^+, extend at least *twice* as far as the maximum holdable equilibrium limits. In other words, the time-optimal trajectory of any holdable setpoint to any other holdable setpoint will be governed by only the first set of switching curves. Therefore, we will focus our efforts on the set of initial conditions for which the first two switching curves alone are sufficient, which can be described more formally as

$$\begin{split}\mathcal{Q} = \{x_e : \psi c\bar{u}^- < x_{1e} < \psi c\bar{u}^+ \text{and } x_{2e} \text{ s.t. } x_e \\ \text{can be driven to } \mathcal{S}_1 \text{ in } t < \pi/\omega_d \text{ seconds}\}.\end{split} \tag{21}$$

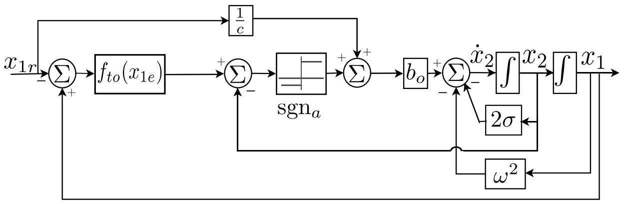

Fig. 3: Block diagram of time-optimal reference tracking controller.

Rather than ignore initial conditions outside $\mathcal{Q}$, we can simplify the control law while keeping it globally defined by letting

$$f_{to}^+ = 0,\ x_{1e} > \psi c\bar{u}^+ \tag{22}$$

$$f_{to}^- = 0,\ x_{1e} < \psi c\bar{u}^-. \tag{23}$$

We prove in Section V that this flattening of the switching curve outside $\mathcal{Q}$ leads to global stability when $\zeta = 0$. This approximation far from the origin was suggested in [12]. We emphasize that for every initial condition in $\mathcal{Q}$, which includes all holdable setpoints, this will still result in a time-optimal trajectory.

Finally, though the input to the error dynamics is $\bar{u} \in [\bar{u}^-,\ \bar{u}^+]$, the input to the actual plant is still $u \in [-u^+,\ +u^+]$, which we obtain by adding back the required steady-state feedforward input, $u_{ss} = \frac{x_{1r}}{c}$. This development can be implemented as the feedback control law

$$u = \text{sgn}_a[-x_{2e} + f_{to}(x_{1e})] + \frac{x_{1r}}{c}, \tag{24}$$

where $f_{to} = f_{to}^- \cup f_{to}^+$. The control law is illustrated in the block diagram shown in Fig. 3. The scheme has the desirable feature that it applies the necessary constant control to hold the state at $x(t) = x_r,\ \forall\, t \geq t_f$.

In the case that $\zeta = 0$, we can explicitly eliminate time from (18) which gives

$$f_{to} = \begin{cases} 0, & x_{1e} < 2c\bar{u}^- \\ \omega\sqrt{2c\bar{u}^- x_{1e} - x_{1e}^2}, & 2c\bar{u}^- \leq x_{1e} < 0 \\ -\omega\sqrt{2c\bar{u}^+ x_{1e} - x_{1e}^2}, & 0 \leq x_{1e} \leq 2c\bar{u}^+ \\ 0, & x_{1e} > 2c\bar{u}^+. \end{cases} \tag{25}$$

Here, f_{to}^- is an ellipse in the negative x_{1e} half-plane, located with a center at $c\bar{u}^-$ with a semi-minor[1] axis length of $c|\bar{u}^-|$, while f_{to}^+ is an ellipse in the positive x_{1e} half-plane which has a center of $c\bar{u}^+$ and a semi-minor axis length of $c\bar{u}^+$ so that in general, each ellipse has a different size and a different center. Only in the regulator case, when $x_r = 0$ and $\bar{u}^- = -u^+$ and $\bar{u}^+ = +u^+$ will the switching curve exhibit symmetry.

B. Time-Optimal Issues

Although time-optimal when $x_{1e}(0) \in \mathcal{Q}$, the controller given by (24) and (25) is impractical to implement. On real systems, there will be process noise, model uncertainties,

---

[1] Throughout this paper, we use "semi-minor axis" to refer to the axis of an ellipse aligned with the x_1-axis of the phase plane. In the ellipses we consider, this terminology is correct provided $\omega > 1$.

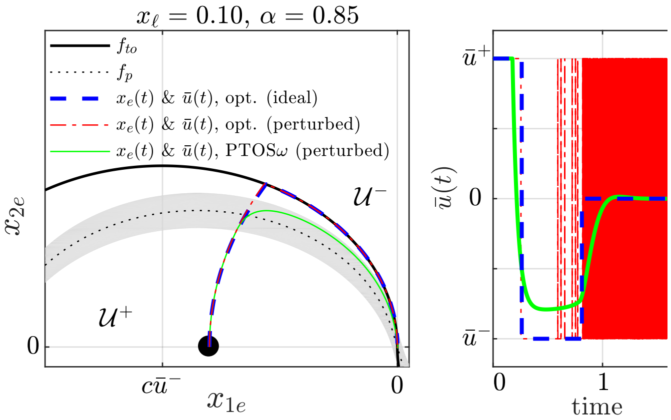

Fig. 4: The solid black curve is f_{to}, the time-optimal switching curve. Under ideal conditions (the dashed blue curve), a trajectory is driven toward f_{to}, at which point the control switches and the trajectory perfectly tracks f_{to} to the origin. The dash-dotted red trajectory illustrates the chattering that occurs with a 5% variation in b_o. In contrast, the solid green trajectory results from the PTOSω control law. The lightly shaded region represents the unsaturated region around f_p, which is defined in (47).

finite actuation bandwidth and delay. These imperfections will contribute to the system chattering as it attempts to follow the final switching curve to the origin. This phenomenon is illustrated in Fig. 4 for a plant with a 5% deviation in b_o. In many systems, such chattering is undesirable, as it can cause physical damage, uses excess control energy, and can excite high-frequency un-modeled dynamics [31, ch. 14], [32, ch. 7]. Moreover, if actuator delays are significant, chattering also leads to reduced control accuracy [31], in contrast to the clean system output seen in Fig. 4.

Similar chattering is observed in sliding mode control (SMC) and much work has been done on SMC to mitigate these problems. Much of that work has focused on linear switching surfaces [31]–[34], and although some SMC studies have considered more general non-linear surfaces [35]–[37], many of these methods do not specifically account for control saturation and special care must be taken in that case [35], [38]. To our knowledge, there is no general SMC chatter reduction method which accounts for the peculiarities of time-optimal control—a situation where the control saturates, the switching surface is not Lipschitz (for both the rigid-body and harmonic oscillator cases), and where motion along the surface requires application of the full control authority.

The chattering problem in time-optimal control has been successfully addressed for a large class of systems exhibiting a rigid-body mode with PTOS-like controllers. It has been noted before that these methods bear a similarity to SMC with a boundary layer where the sliding surface is a *modified* version of the time-optimal surface [32]. In this paper, we build on the classic rigid-body PTOS methods to develop similar controllers, which we call PTOSω and PTOS$\omega\zeta$ (collectively, PTOS$\omega(\zeta)$), for the oscillatory system described by (2)-(3). With foresight, Fig. 4 also shows the trajectory in the phase plane subjected to the PTOSω control law. We begin by deriving a special case of PTOS$\omega(\zeta)$, the regulator.

III. PTOS$\omega(\zeta)$: REGULATOR

In this section, we develop the PTOS$\omega(\zeta)$ for (2)-(3) for the special regulator case. In this case, $x_{1r} = 0$, $\bar{u}^- = -u^+$, $\bar{u}^+ = +u^+$ and the switching curves are symmetric as seen in Fig. 2. For this derivation, we use the symmetric signum function, $\text{sgn}(\cdot)$, because the control limits are now symmetric.

To motivate the development, note that after the last switch, the time-optimal control law, (24), can be seen as tracking an optimal velocity profile $f_{to}^{\pm}$, that has infinite slope at the origin. As with the rigid body PTOS [16], the PTOS$\omega(\zeta)$ seeks to approximate the optimal control by first replacing the infinite gain of the $\text{sgn}(\cdot)$ function with a large yet finite gain and a saturator. Second, the optimal velocity profile f_{to} is replaced with an approximation, f_{pr} (termed *the PTOS function*) with two key differences: (i) near the origin, the optimal velocity profile is approximated with a constant, finite slope, yielding a linear feedback region, and (ii) the optimal velocity profile is discounted by a factor $\alpha \in (0, 1)$.

The discount factor has been shown to increase robustness against un-modeled dynamics in the rigid-body case [17], [25], though we will not pursue the issue here. The discount factor is typically also a prerequisite for constructing an invariant region about f_{pr} [16], which we will show is also the case here when we prove stability for PTOSω in Section V-A. Additionally, in the rigid-body PTOS, decreasing the discount factor α results in an increased closed-loop damping within the linear region and has been used as a tuning parameter to help mitigate overshoot [20], [39]. We derive a similar relationship for PTOSω in Section VI.

In the stability proof for PTOSω, we will require $\alpha \in (1/2, 1)$.[2] Typically, $\alpha \in (0, 1)$ in rigid-body PTOS controllers [16], [25]. If we discount the available acceleration by a factor α, then $f_{to}(x_1)$ scales according to $u^+ \leftarrow \alpha u^+$, which can be seen by integrating (17) backwards with $u(t) = \pm u^+ \alpha$. Thus, the ellipse described by the discounted velocity profile has an x_1-axis length of $2\alpha c u^+$. Requiring $\alpha > 1/2$ has the following effect: when subjected to $u = +u^+$ (resp., $u = -u^+$), the system rotates in an ellipse about the rotation center $(+cu^+, 0)$ (resp., $(-cu^+, 0)$). By fixing $\alpha > 1/2$, we ensure that this rotation center is always *inside* the endpoints of the discounted velocity profile. As we show in Section V, this permits a globally stable controller.

A. *Development of* $f_{pr}(x_1)$

Let $\hat{f}_{to}^{\pm}(x_1)$ be the discounted optimal velocity profile, obtained by replacing $\bar{u}^{\pm}$ with $\alpha\bar{u}^{\pm}$ in (18), (22), (23). This change will shrink the x_1-axis length of the discounted velocity profile from $\psi c u^+$ to $\psi \alpha c u^+$, as illustrated in Fig. 5. Consider the controller given by,

$$u_{pr}(t) = \begin{cases} \text{sat}\big[k_2(-x_2 + f_{pr}(x_1))\big], & |x_1| < \psi\alpha c u^+ \\ u^+\text{sgn}(-x_2 + f_{pr}(x_1)), & \text{otherwise} \end{cases} \tag{26}$$

---

[2] This restriction can evidently be relaxed somewhat in the damped case, because as ζ increases, the distance of the end-points of the switching curve from the rotation centers $(\alpha c\bar{u}^{\pm}, 0)$ increases.

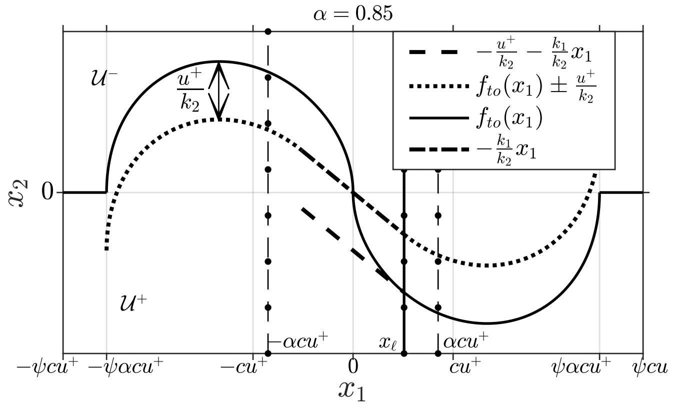

Fig. 5: Illustration of the development of $f_{pr}(x_1)$. The solid black curve depicts $\hat{f}_{to}(x_1)$ and the dashed curve is the Taylor approximation of $\hat{f}_{to}(x_1)$ about x_ℓ. We shift this dashed curve up by $\frac{u^+}{k_2}$, giving $f_\ell(x_1)$ (dash-dotted). Then, from $[x_\ell, \psi\alpha c u^+]$, we shift $\hat{f}_{to}$ up by $\frac{u^+}{k_2}$; and from $[-\psi\alpha c u^+, -x_\ell]$, we shift $\hat{f}_{to}$ down by $\frac{u^+}{k_2}$, which are the dotted curves. This gives $f_{pr}(x_1)$ as the concatenation of the dotted and dash-dotted curves.

where

$$\text{sat}(\xi) = \begin{cases} u^+ & \xi \geq u^+ \\ \xi & |\xi| < u^+ \\ -u^+ & \xi \leq -u^+. \end{cases} \tag{27}$$

When $|x_1| < \psi\alpha c u^+$, $f_{pr}(x_1)$ is an approximation to the optimal velocity profile, $f_{to}(\cdot)$. The derivation of $f_{pr}(x_1)$ is the main focus of this section. First, note that a saturator and a gain gives a finite slope approximation to the sgn$(\cdot)$ function. By making $f_{pr}(x_1)$ approximate $f_{to}(x_1)$ and making k_2 large, then in (26) we have an approximation to the optimal control, (24). Furthermore, we can employ a linear feedback controller near the origin (i.e., for $|x_1| \leq x_\ell$) by defining $f_{pr}(x_1)$ as the piecewise function

$$f_{pr}(x_1) = \begin{cases} f_\ell(x_1), & |x_1| \leq x_\ell \\ f_{n\ell}(x_1), & x_\ell < |x_1| \leq \psi\alpha c u^+ \\ 0 & |x_1| > \psi\alpha c u^+ \end{cases} \tag{28}$$

where we require that

$$f_\ell(x_\ell) = f_{n\ell}(x_\ell) \tag{29}$$

$$f'_\ell(x_\ell) = f'_{n\ell}(x_\ell), \tag{30}$$

where the primes in (30) indicate differentiation with respect to x_1. By making $f_\ell(x_1)$ a *linear* function of x_1, then for $|x_1| \leq x_\ell$, (26) describes the familiar equation for linear state feedback, with the sat$(\cdot)$ function enforcing respect for the control limits. Specifically, define the linear portion of f_{pr} as

$$f_\ell(x_1) := -\Big(\frac{k_1}{k_2}\Big)x_1, \quad |x_1| < x_\ell. \tag{31}$$

We construct the entire $f_{pr}(x_1)$ by connecting this linear f_ℓ to vertical translations of $\hat{f}_{to}$ such that (29) and (30) are satisfied. Taking the Taylor approximation of (25) about x_ℓ yields

$$\hat{f}_{to}(x_1) \approx -\frac{u^+}{k_2} - \frac{k_1}{k_2}x_1. \tag{32}$$

The slope $-k_1/k_2$ is found as a combined quantity by evaluating the derivative of $\hat{f}_{to}$ at x_ℓ. This is done by noting from (20) that $\dot{\hat{f}}_{to} = \hat{f}'_{to}(x_1)\dot{x}_1$ and also that $\dot{x}_2 = \dot{\hat{f}}_{to}$. Since the control input which defined $\hat{f}_{to}$ is constant (i.e., $\pm\alpha u^+$), we can explicitly solve for $\hat{f}'_{to}(x_1)$ and hence the slope, $-k_1/k_2$, as

$$-\frac{k_1}{k_2} := \hat{f}'_{to}(x_\ell) = \frac{-\omega^2 x_\ell - 2\sigma\hat{f}_{to}(x_\ell) + b_o\alpha u^+}{\hat{f}_{to}(x_\ell)} \tag{33}$$

where we have used $\dot{x}_1 = x_2 = \hat{f}_{to}$. Evaluating (32) at x_ℓ and solving for the x_2 intercept, $-u^+/k_2$, yields

$$-\frac{u^+}{k_2} = \hat{f}_{to}(x_\ell) + \frac{k_1}{k_2}x_\ell, \tag{34}$$

so that

$$k_2 = \frac{-u^+}{\hat{f}_{to}(x_\ell) + (k_1/k_2)x_\ell}. \tag{35}$$

We find k_1 by negating the product of (35) and (33),

$$k_1 = -f'_{to}(x_\ell)k_2. \tag{36}$$

The dashed curve in Fig. 5 is (32). Since our new velocity profile must go through the origin, add the x_2-intercept, $\frac{u^+}{k_2}$, to (32) to yield $f_\ell(x_1)$, the dash-dotted curve in Fig. 5. We connect the parts of $\hat{f}_{to}$ outside $[-x_\ell,\, x_\ell]$ to f_ℓ by shifting the right portion of $\hat{f}_{to}$ *up* by $\frac{u^+}{k_2}$ and the left portion *down* by $\frac{u^+}{k_2}$, which is the dotted curve. Together, this yields the concatenation of the dash-dotted and dotted curves in Fig. 5, which is $f_{pr}(x_1)$. We thus obtain

$$f_\ell(x_1) = -\frac{k_1}{k_2}x_1 \tag{37}$$

$$f_{n\ell}(x_1) = \hat{f}_{to}(x_1) + \text{sgn}(x_1)\frac{u^+}{k_2}. \tag{38}$$

Remark: It is clear that if $\alpha \to 1$, then $\hat{f}_{to} \to f_{to}$. For $x_1 \in (0, c\alpha u^+)$, it is fairly straightforward to show that $f''_{to}(x_1)$ is positive which implies $f_{to}(x_1)$ is convex on that interval. Thus, evaluating the linear approximation of f_{to}, which is given by (32), at zero implies $-u^+/k_2 \leq f_{to}(0) = 0$. If $0 < x_\ell < c\alpha u^+$, then $k_1/k_2 > 0$ and hence,

$$0 \geq -\frac{u^+}{k_2} \tag{39}$$

$$\geq -\frac{u^+}{k_2} - \frac{k_1}{k_2}x_\ell = f_{to}(x_\ell). \tag{40}$$

Since $f_{to}(x_\ell) \to 0$ as $x_\ell \to 0$ it follows that as $x_\ell \to 0$, $u^+/k_2 \to 0$ and thus $k_2 \to \infty$ and we recover (24).

IV. PTOS$\omega(\zeta)$: REFERENCE TRACKING

Inspired by the development of the regulator PTOS$\omega(\zeta)$, we now develop the setpoint tracking PTOS$\omega(\zeta)$. Deriving the setpoint tracking PTOS$\omega(\zeta)$ function $f_p(x_{1e})$ proceeds similarly, though examining Fig. 1, the first challenge immediately presents itself. If we are to maintain the continuous differentiability of $f_p(x_{1e})$, we cannot have $|x_\ell^-| = x_\ell^+$, since at a single x_ℓ the curves $\hat{f}_{to}^-$ and $\hat{f}_{to}^+$ have different slopes, i.e., $\hat{f}_{to}'^-(-x_\ell) \neq \hat{f}_{to}'^+(x_\ell)$. Instead, because the curves are geometrically similar, we choose x_ℓ^- and x_ℓ^+ as a *fraction* of the distance to the rotation centers. That is, for $0 < \lambda < 1$, choose[3]

$$x_\ell^+ = \lambda\alpha c\bar{u}^+ \tag{41}$$

$$x_\ell^- = \lambda\alpha c\bar{u}^-. \tag{42}$$

The following lemma establishes that this yields $\hat{f}_{to}'(x_\ell^+) = \hat{f}_{to}'(x_\ell^-)$.

Lemma 1: Let x_ℓ^+ and x_ℓ^- be given by (41) and (42), respectively. Then $\hat{f}_{to}'(x_\ell^+) - \hat{f}_{to}'(x_\ell^-) = 0$.

Proof: Recalling the definitions of $\bar{u}^\pm$ in (8)-(9), we can calculate $\hat{f}_{to}'(x_\ell^+)$ using (33) by replacing x_ℓ and u^+ with $\lambda\alpha c\bar{u}^+$ and $\bar{u}^+$, respectively. To find $\hat{f}_{to}'(x_\ell^-)$, we similarly substitute $\lambda\alpha c\bar{u}^-$ and $\bar{u}^-$. Also using (18), we then have

$$\begin{aligned} \hat{f}_{to}'(x_\ell^+) - \hat{f}_{to}'(x_\ell^-) =& \alpha\bar{u}^+ \frac{-\omega^2 c\lambda + b_o}{\hat{f}_{to}(\lambda\alpha c\bar{u}^+)} - \alpha\bar{u}^- \frac{-\omega^2 c\lambda + b_o}{\hat{f}_{to}(\lambda\alpha c\bar{u}^-)} & (43) \\ =& (-\omega^2 c\lambda + b_o)\left(\frac{\alpha\bar{u}^+}{x_{2e}^*(t_k^+)} - \frac{\alpha\bar{u}^-}{x_{2e}^*(t_k^-)}\right) & (44) \end{aligned}$$

for some t_k^+ and t_k^- such that $x_{1e}^*(t_k^+) = \lambda\alpha c\bar{u}^+$ and $x_{1e}^*(t_k^-) = \lambda\alpha c\bar{u}^-$. Because $\alpha\bar{u}^\pm$ scales $x_{2e}^*(t_k^\pm)$, the fractions in (44) become normalized so it only remains to show that $t_k^+ = t_k^-$. But from (18), $\alpha\bar{u}^\pm$ also scales $x_{1e}^*(t_k^\pm)$. Hence, the equality $x_{1e}^*(t_k^\pm) = \lambda\alpha c\bar{u}^\pm$ is completely independent of the factors $\alpha\bar{u}^+$ and $\alpha\bar{u}^-$ and the equality of the t_k follows from their uniqueness. ■

Thus, we define $k_1/k_2 := -\hat{f}_{to}'^-(x_\ell^-) = -\hat{f}_{to}'^+(x_\ell^+)$. Associate gain k_2^+ with the positive x_{1e} half-plane and k_2^- with the negative x_{1e} half-plane. Then for some small perturbation $\delta x_{1e} = x_{1e} - x_\ell^+$ (resp., $\delta x_{1e} = x_{1e} - x_\ell^-$), in the vicinity of x_ℓ^+ (resp., x_ℓ^-) we have

$$\hat{f}_{to}(x_\ell^- + \delta x_{1e}) \approx -\frac{\bar{u}^-}{k_2^-} - \left(\frac{k_1}{k_2}\right) x_{1e} \tag{45}$$

$$\hat{f}_{to}(x_\ell^+ + \delta x_{1e}) \approx -\frac{\bar{u}^+}{k_2^+} - \left(\frac{k_1}{k_2}\right) x_{1e}. \tag{46}$$

The same argument used to show (44) is equal to zero in Lemma 1 will also show that $k_2^+ = k_2^-$. Thus, we define $k_2 := k_2^+ = k_2^-$. Using this definition and evaluating (45) and (46) at $\delta x_{1e} = 0$, we obtain the two x_{2e}-intercepts,

$$\begin{aligned} -\frac{\bar{u}^-}{k_2} &= \hat{f}_{to}(x_\ell^-) + \left(\frac{k_1}{k_2}\right) x_\ell^- \\ -\frac{\bar{u}^+}{k_2} &= \hat{f}_{to}(x_\ell^+) + \left(\frac{k_1}{k_2}\right) x_\ell^+. \end{aligned}$$

With analogy to Section III-A, the x_{2e}-intercepts are subtracted off from (45) and (46) to obtain the linear portion of $f_p(x_{1e})$, which yields a single linear curve between x_ℓ^- and x_ℓ^+. Similarly, we shift $\hat{f}_{to}$ down by $|\bar{u}^-|/k_2$ for $x_{1e} \in (\psi c\alpha\bar{u}^-, x_\ell^-)$ and up by $\bar{u}^+/k_2$ for $x_{1e} \in (x_\ell^+, \psi c\alpha\bar{u}^+)$ to obtain the non-linear portion of $f_p(x_{1e})$. This yields f_p as

$$f_p(x_{1e}) = \begin{cases} 0, & x_{1e} < \psi c\alpha\bar{u}^- \\ \hat{f}_{to}(x_{1e}) + \frac{\bar{u}^-}{k_2}, & \psi c\alpha\bar{u}^- \leq x_{1e} \leq x_\ell^- \\ -\frac{k_1}{k_2} x_{1e}, & x_\ell^- < x_{1e} < x_\ell^+ \\ \hat{f}_{to}(x_{1e}) + \frac{\bar{u}^+}{k_2}, & x_\ell^+ \leq x_{1e} \leq \psi c\alpha\bar{u}^+ \\ 0, & x_{1e} > \psi c\alpha\bar{u}^+. \end{cases} \tag{47}$$

Thus the PTOS$\omega(\zeta)$ control for the error dynamics is given by

$$\bar{u}_p = \begin{cases} \operatorname{sgn}_a(-x_{2e} + f_p(x_{1e})) & x_{1e} < \psi c\alpha\bar{u}^- \\ \operatorname{sat}_a\{k_2[-x_{2e} + f_p(x_{1e})]\} & x_{1e} \in [\psi c\alpha\bar{u}^-, \psi c\alpha\bar{u}^+] \\ \operatorname{sgn}_a(-x_{2e} + f_p(x_{1e})) & x_{1e} > \psi c\alpha\bar{u}^+, \end{cases} \tag{48}$$

where the asymmetric saturator is given by

$$\operatorname{sat}_a(\xi) = \begin{cases} \bar{u}^+, & \xi > \bar{u}^+ \\ \xi, & \bar{u}^- \leq \xi \leq \bar{u}^+ \\ \bar{u}^-, & \xi < \bar{u}^-. \end{cases} \tag{49}$$

Just as in the time-optimal case, we add back the required steady-state feedforward control which yields

$$u_p = \bar{u}_p + \frac{x_{1r}}{c}. \tag{50}$$

V. STABILITY OF THE REFERENCE TRACKING PTOSω

In this section, we prove stability for the case that $\zeta = 0$, an assumption we maintain for the next two sections. In this case, the gains k_1 and k_2 can be calculated as

$$k_1 = \frac{1-\lambda}{\alpha c\lambda}, \tag{51}$$

$$k_2 = \frac{\sqrt{2\lambda - \lambda^2}}{\omega\alpha c\lambda}. \tag{52}$$

---

[3] The PTOSω stability condition CII of Theorem 1 in Section V will further restrict λ by the size of the setpoint, with an upper limit of $\lambda = 0.4$ when the setpoint is zero.

It will be useful to define the following divisions of the error-coordinate state space:

$$\begin{aligned}
\mathcal{P} &= \Big\{x_e \colon \frac{\bar{u}^-}{k_2} \le (-x_{2e} + f_p(x_{1e})) \le \frac{\bar{u}^+}{k_2}, \\
&\qquad x_{1e} \in [2\alpha c\bar{u}^-, 2\alpha c\bar{u}^+]\Big\} \\
\mathcal{T}^+ &= \big\{x_e \colon x_e \in \mathcal{P},\ x_{1e} > \alpha c\bar{u}^+, x_{2e} > 0\big\} \\
\mathcal{T}^- &= \big\{x_e \colon x_e \in \mathcal{P},\ x_{1e} < \alpha c\bar{u}^-, x_{2e} < 0\big\} \\
\mathcal{B} &= \big\{x_e \colon x_e \in \mathcal{P} \setminus (\mathcal{T}^- \cup\ \mathcal{T}^+)\big\} \\
\mathcal{L}^- &= \big\{x_e \colon x_e \in B,\ \ x_{1e} \in [x_\ell^-, 0]\big\} \\
\mathcal{L}^+ &= \big\{x_e \colon x_e \in B,\ \ x_{1e} \in [0, x_\ell^+]\big\} \\
\mathcal{L} &= \mathcal{L}^- \cup \mathcal{L}^+ \\
\mathcal{U}^- &= \big\{x_e \colon x_e \notin \mathcal{P},\ \ x_{2e} \ge f_p(x_{1e})\big\} \\
\mathcal{U}^+ &= \big\{x_e \colon x_e \notin \mathcal{P},\ \ x_{2e} \le f_p(x_{1e})\big\}.
\end{aligned}$$

These regions are illustrated in Fig. 7. Regions $\mathcal{U}^+$ and $\mathcal{U}^-$ are the regions of the state space which result in a saturated control. The entire region $\mathcal{P}$ results in an unsaturated control. The region $\mathcal{B}$ is an invariant subset of $\mathcal{P}$, though the "tails" of $\mathcal{P}$, called, $\mathcal{T}^\pm$ are not invariant. Together, $\mathcal{T}^- \cup \mathcal{B} \cup \mathcal{T}^+ = \mathcal{P}$. Finally, $\mathcal{L} \subset \mathcal{B} \subset \mathcal{P}$, where $\mathcal{L}$ defines the region of unsaturated linear feedback.

Theorem 1: If the system described by (7) with $\zeta = 0$ under the control law given by (47)–(49) satisfies

CI) $1/2 < \alpha < 1$,

CII) $|\gamma| < 1 - \frac{2\lambda}{\sqrt{2\lambda - \lambda^2}}$,

CIII) $\left(\frac{u^+}{k_2}\right)^2 < \frac{c^2\omega^2}{4}R$, where

$$R = \min\{R^+,\ R^-\} \tag{53}$$

$$R^+ = \big(2\bar{u}^+ - (\alpha+1)\bar{u}^-\big)^2 - \big(2\alpha\bar{u}^+ - \bar{u}^-\big)^2 \tag{54}$$

$$R^- = \big((\alpha+1)\bar{u}^+ - 2\bar{u}^-\big)^2 - \big(2\alpha\bar{u}^- - \bar{u}^+\big)^2 \tag{55}$$

then the system is globally asymptotically stable about the origin of the x_e phase plane.

Proof: Lemma 2 establishes that all trajectories enter region $\mathcal{P}$ in finite time. Theorem 2 establishes that region $\mathcal{B}$ is invariant. Lemma 9 establishes that all trajectories in $\mathcal{T}^+$ (resp., $\mathcal{T}^-$) will leave $\mathcal{T}^+$ (resp., $\mathcal{T}^-$) and enter $\mathcal{B}$ in finite time. Finally, Theorem 3 shows that region $\mathcal{B}$ is asymptotically stable about the origin by developing a Lyapunov function. ■

Lemma 2: Given an initial condition $x(0) = x_0 \notin \mathcal{P}$, the system described by (7) under the control law given by (48) will drive the system to region $\mathcal{P}$ in finite time.

Proof: Because the state rotates clockwise at a rate of ω in the phase space and $f_p(x_{1e})$ divides the phase space into two disjoint regions, then after $t < 2\pi/\omega$ units of time any trajectory under a constant input must cross $f_p(x_{1e})$.

Case 1: If the initial condition is such that, in $t < 2\pi/\omega$ units of time, the trajectory crosses $f_p(x_{1e})$ with $2\alpha c\bar{u}^- \le x_{1e} \le 2\alpha c\bar{u}^+$, we are done.

Case 2: Otherwise, the trajectory crosses $f_p(x_{1e})$ where $f_p(x_{1e}) = 0$. Hence, it is sufficient to show that all initial conditions of the form

$$x_e(0) = [x_{1e}^o, 0]^T, x_{1e}^o \notin [2\alpha c\bar{u}^-,\ 2\alpha c\bar{u}^+] \tag{56}$$

enter $\mathcal{P}$ in finite time.

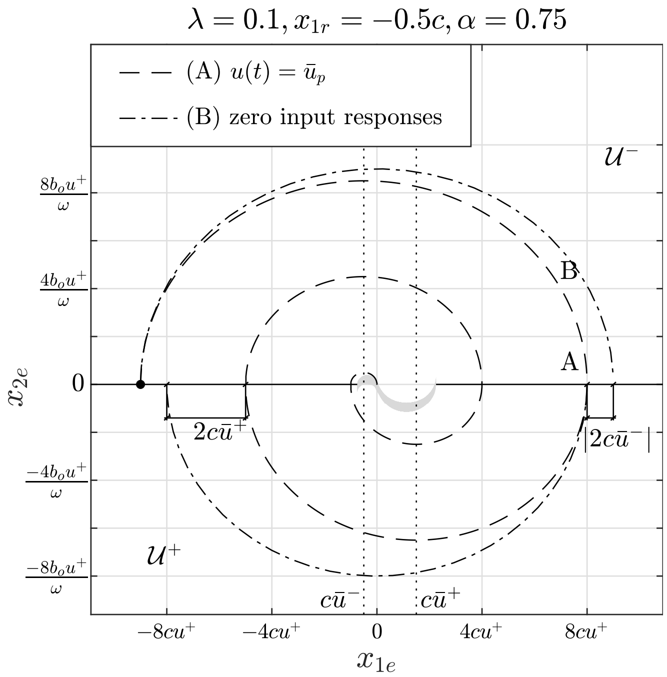

Fig. 6: Trajectory (B) shows the state evolving with zero input. Compare this to the bang-bang trajectory, (A), where the control alternately decreases the magnitude of x_{1e} by $|2c\bar{u}^-|$ then $2c\bar{u}^+$.

When $\bar{u}_p(t)$ is held constant at $\bar{u}_p = \bar{u}^+$ (resp., $\bar{u}_p = \bar{u}^-$), it is straightforward to show using (4) and (5) that the resulting trajectory describes a portion of an ellipse centered at $(+c\bar{u}^+,\ 0)$ (resp., $(c\bar{u}^-,\ 0)$). It follows that between every switch (besides the first and last), the absolute distance of x_1 to the origin has decreased by $2c\bar{u}^+$(resp., $|2c\bar{u}^-|$).

If the trajectory crosses the x_{1e}-axis with $2\alpha c\bar{u}^+ < x_{1e} < 2c\bar{u}^+$ (resp., $2c\bar{u}^- < x_{1e} < 2\alpha c\bar{u}^-$), then the restriction that $0.5 < \alpha < 1$ ensures that the rotation center, $c\bar{u}^-$ (resp., $c\bar{u}^+$) is contained between the endpoints of region $\mathcal{P}$, so that the trajectory must intersect the boundary of $\mathcal{P}$. The significance of this can be seen in Fig. 6. If we allowed $\alpha \le 1/2$, then at the final switch before entering $\mathcal{P}$, the ellipse described by the trajectory could (with the right initial condition) rotate about a point *outside* $\mathcal{P}$ and the state would never enter $\mathcal{P}$.

Finally, after $2\pi/\omega$ units of time, i.e., after every two switches, the absolute distance of x_{1e} from the origin decreases by $4cu^+$ so that any state within a finite distance must enter $\mathcal{P}$ in finite time. ■

A. The Region $\mathcal{B}$ Is Invariant

Theorem 2: The region $\mathcal{B}$ is an invariant set, i.e., once a trajectory enters $\mathcal{B}$ the state is trapped there.

Proof: Considering Fig. 7, we see that the long upper and lower boundaries of $\mathcal{B}$ are given by the segments $\bar{D}C$ and $\bar{C}D$, which separate $\mathcal{B}$ from $\mathcal{U}^\pm$. The shorter segments, $\bar{D}\bar{C}$ and CD, separate $\mathcal{B}$ from $\mathcal{T}^\pm$. To show that $\mathcal{B}$ is invariant, we show that at every point on the boundary, the vector field points toward the interior of $\mathcal{B}$. Lemmas 4-7 below establish

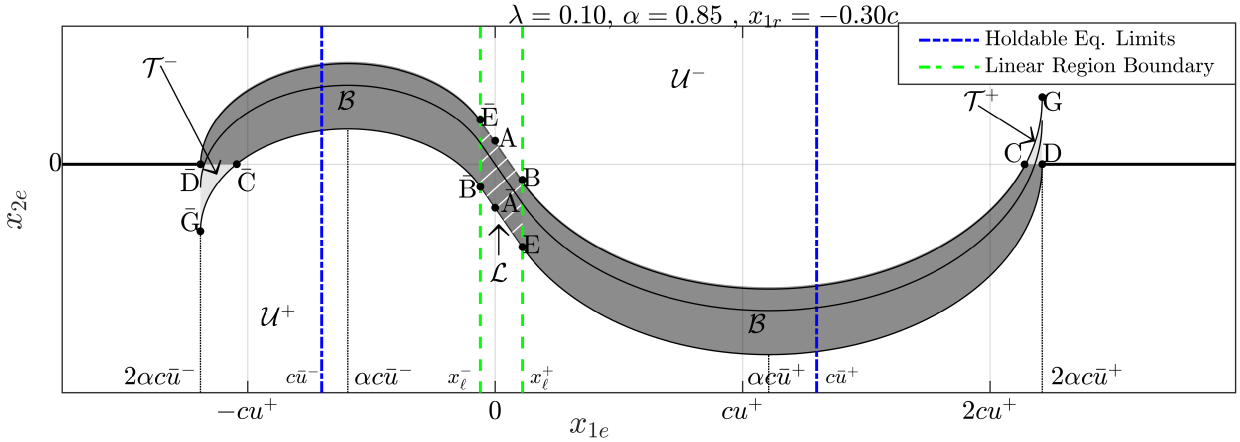

Fig. 7: The entire shaded region is $\mathcal{P}$, where the control is unsaturated. The lightly shaded tails are $\mathcal{T}^\pm$. The darkly shaded region together with the hatch-marked region is $\mathcal{B}$, which is invariant. The hatch-marked region is $\mathcal{L} \subset \mathcal{B}$.

this fact for segments $\bar{D}C$ and $\bar{C}D$. Lemma 8 shows this also holds for the boundary between $\mathcal{B}$ and $\mathcal{T}^\pm$. ■

To show that trajectories move to the interior of $\mathcal{B}$ at the boundaries between $\mathcal{B}$ and $\mathcal{U}^\pm$, we will consider the time derivative of $\bar{u}_p(t)$ along trajectories of the system evaluated at these upper and lower boundaries. For the system to remain trapped, we must have that on the upper boundary ($\bar{D}C$), $\dot{\bar{u}}_p(x_e(t)) > 0$; and on the lower boundary ($\bar{C}D$), $\dot{\bar{u}}_p(x_e(t)) < 0$ (this implies the magnitude of the control is receding from its saturated value, and hence the trajectory is moving toward toward the interior of $\mathcal{B}$). To start, we take the time derivative of $\bar{u}_p(x_e(t))$ along a trajectory. This yields

$$\begin{aligned}\dot{\bar{u}}_p(t) =& k_2 f_p'(x_{1e}) f_p(x_{1e}) - f_p'(x_{1e})\bar{u}_p(t) \\ &+ k_2\omega^2 x_{1e} - k_2 b_o \bar{u}_p(t). \end{aligned} \tag{57}$$

If we consider this derivative evaluated on either the upper or lower boundary of $\mathcal{B}$, we have $\bar{u}_p(t) = \bar{u}^-$ and $\bar{u}_p(t) = \bar{u}^+$, respectively. Let $\dot{\bar{u}}_u(t)$ and $\dot{\bar{u}}_\ell(t)$ denote the time derivatives of $\bar{u}_p(t)$ along the upper and lower boundary of $\mathcal{B}$, respectively. Then for invariance, the following inequalities must hold

$$\begin{aligned}\dot{\bar{u}}_u(t) =& k_2 f_p'(x_{1e}) f_p(x_{1e}) - f_p'(x_{1e})\bar{u}^- \\ &+ k_2\omega^2 x_{1e} - k_2 b_o \bar{u}^- > 0 \end{aligned} \tag{58}$$

$$\begin{aligned}\dot{\bar{u}}_\ell(t) =& k_2 f_p'(x_{1e}) f_p(x_{1e}) - f_p'(x_{1e})\bar{u}^+ \\ &+ k_2\omega^2 x_{1e} - k_2 b_o \bar{u}^+ < 0. \end{aligned} \tag{59}$$

Before stating and proving Lemmas 4-8, we note for $x \in \mathcal{P}$

$$f_p'(x_{1e}) = \begin{cases} \frac{\omega(\alpha c\bar{u}^- - x_{1e})}{\sqrt{2\alpha c\bar{u}^- x_{1e} - x_{1e}^2}} & 2\alpha c\bar{u}^- \leq\ x_{1e}\ \leq x_\ell^- \\ -\frac{k_1}{k_2} & x_\ell^- < |x_{1e}| < x_\ell^+ \\ -\frac{\omega(\alpha c\bar{u}^+ - x_{1e})}{\sqrt{2\alpha c\bar{u}^+ x_{1e} - x_{1e}^2}} & x_\ell^+ \leq\ x_{1e}\ \leq 2\alpha c\bar{u}^+. \end{cases} \tag{60}$$

Another useful observation is

Lemma 3: For $x_{1e} > 0$, $f_p'(x_{1e})$ is monotonically increasing; and for $x_{1e} < 0$, $f_p'(x_{1e})$ is monotonically decreasing.

Proof: Note that $f_p''(x_{1e}) = 0$ for $x_{1e} \in \mathcal{L}$. Thus, we need only show that $\frac{d}{dx_{1e}} f_p'(x_{1e}) > 0$ over the entire interval $x_{1e} \in [x_\ell^+, 2\alpha c\bar{u}^+]$. Calculating the derivative, we see that

$$f_p''(x_{1e}) = \frac{\omega}{\sqrt{2\alpha c\bar{u}^+ x_{1e} - x_{1e}^2}} + \frac{\omega(\alpha c\bar{u}^+ - x_{1e})^2}{(2\alpha c\bar{u}^+ x_{1e} - x_{1e}^2)^{3/2}}. \tag{61}$$

Both terms are always positive and real when $0 < x_\ell^+ \leq x_{1e} \leq 2\alpha c\bar{u}^+$, as desired. The case for negative x_{1e} follows similarly. ■

Throughout the rest of the section, we will reference Fig. 7, which shows the boundaries of region $\mathcal{B}$ divided into different sections which we consider separately. However, even though the curves are not strictly symmetric, there is an equivalence between, for example, segment BC and $\bar{C}\bar{B}$. These equivalent segments are considered concurrently in the ensuing proofs.

Lemma 4: Inequality (59) holds for segment ED (the lower boundary in the non-linear region for positive x_{1e}) and (58) holds for segment $\bar{D}\bar{E}$ (the upper boundary in the non-linear region for negative x_{1e}).

Proof: Using (47) and (60) in (57), we obtain

$$\begin{aligned}\dot{\bar{u}}_p &= k_2 b_o \alpha \bar{u}^\pm - k_2 b_o \bar{u}^\pm \\ &= k_2 b_o \bar{u}^\pm(\alpha - 1). \end{aligned} \tag{62}$$

Since $\alpha \in (1/2,\ 1)$ and $\bar{u}^- < 0$ and $\bar{u}^+ > 0$, then both (58) and (59) are satisfied. ■

Lemma 5: In the linear region, inequality (59) holds for $\bar{A}E$ (lower boundary in $\mathcal{L}^+$) and inequality (58) holds for $\bar{E}A$ (upper boundary in $\mathcal{L}^-$).

Proof: First consider the linear region on the lower boundary for $x_{1e} > 0$ (segment $\bar{A}E$). Using (60) and (47) in (59), we obtain

$$k_2 \frac{k_1}{k_2}\frac{k_1}{k_2} x_{1e} + \frac{k_1}{k_2}\bar{u}^+ + k_2\omega^2 x_{1e} - k_2 b_o \bar{u}^+ < 0 \tag{63}$$

We can *maximize* the LHS by letting $x_{1e} = x_\ell^+ = \alpha c\bar{u}^+\lambda$. Furthermore, using the expressions for k_1 and k_2 from (51) and (52), we obtain

$$\omega^2 \frac{(1-\lambda)^2}{(2\lambda-\lambda^2)}\lambda\alpha c\bar{u}^+ + \omega^2\frac{(1-\lambda)}{(2\lambda-\lambda^2)}\alpha c\lambda\bar{u}^+ + \omega^2\alpha c\lambda\bar{u}^+ - b_o\bar{u}^+ < 0 \tag{64}$$

Using $c = b_o/\omega^2$ and canceling $\bar{u}^+$, we obtain, after further algebra

$$(2-\lambda)(\alpha-1) < 0.$$

Because $\lambda < 1$, the first factor is positive while the second factor is always negative. Therefore, the inequality holds.

The result for segment $\bar{E}A$ follows similarly by noting the flip in inequalities that would occur when $\bar{u}^-$ is canceled in (64). Also, note that one would substitute $x_{1e} = \alpha c\lambda\bar{u}^-$ which is negative. ■

Lemma 6: Inequality (58) holds for segment AB (the upper boundary in $\mathcal{L}^+$) and inequality (59) holds for segment $\bar{B}\bar{A}$ (the lower boundary in $\mathcal{L}^-$).

Proof: We begin with the upper boundary for positive x_{1e} (segment AB). For this segment, (58) becomes

$$k_2\left(\frac{k_1}{k_2}\right)^2 x_{1e} + \frac{k_1}{k_2}\bar{u}^- + k_2\omega^2 x_{1e} - k_2 b_o\bar{u}^- > 0. \tag{65}$$

We can minimize the LHS by letting $x_{1e} = 0$. Then (65) can be re-written as

$$\frac{k_1}{k_2^2}(-|\bar{u}^-|) - b_o(-|\bar{u}^-|) > 0. \tag{66}$$

By canceling $|\bar{u}^-|$ and using k_1 and k_2 from (51) and (52) we obtain

$$2 - \lambda(1-\alpha) - \alpha > 0 \tag{67}$$

which holds since λ and α are each less than one. The case for segment $\bar{B}\bar{A}$ follows nearly identically. ■

Lemma 7: In the nonlinear region, inequality (58) holds for segment BC (the upper boundary for positive x_{1e}) and inequality (59) holds for segment $\bar{C}\bar{B}$ (the lower boundary for negative x_{1e}).

Proof: Consider segment BC. Using (47) and (60), (58) becomes

$$\dot{\bar{u}}_u = k_2\alpha b_o\bar{u}^+ + f_p'(x_{1e})(\bar{u}^+ - \bar{u}^-) - k_2 b_o\bar{u}^- > 0. \tag{68}$$

Using the parameterization of $\bar{u}^+$ and $\bar{u}^-$ in (10) and (11), we have

$$u^+\left(k_2\alpha b_o(1-\gamma) + k_2 b_o(1+\gamma) + 2f_p'(x_{1e})\right) > 0. \tag{69}$$

Now, by Lemma 3, $f_p'(x_{1e})$ is monotonically increasing for $x_{1e} > 0$, so that we can minimize the right-hand side by letting $x_{1e} = x_\ell^+ = \lambda\alpha c\bar{u}^+$. This gives

$$\alpha(1-\gamma) + (1+\gamma) - 2\frac{(1-\lambda)}{2-\lambda}\alpha > 0. \tag{70}$$

After some algebra, this becomes

$$(2-\lambda)(1+\gamma-\alpha\gamma) + \alpha\lambda > 0. \tag{71}$$

Since each term is positive, the inequality holds.

The case for $\bar{C}\bar{B}$ follows similarly. ■

Lemma 8: Suppose that Conditions *CI* and *CII* are satisfied. Then (i) the boundary between $\mathcal{B}$ and $\mathcal{T}^+$ (resp., $\mathcal{B}$ and $\mathcal{T}^-$) is a line-segment, $x_2 = 0$, between points CD (resp., $\bar{D}\bar{C}$), and (ii) at this boundary, the vector field points toward the interior of $\mathcal{B}$.

Proof: To show (i), we must ensure that at $x_{1e} = \alpha c\bar{u}^+$, the upper boundary is less than zero; and at $x_{1e} = \alpha c\bar{u}^-$, the lower boundary is greater than zero.

The upper boundary at $x_{1e} = \alpha c\bar{u}^+$ is given by

$$\begin{aligned} x_{2e}^{upper} &= -\frac{\bar{u}^-}{k_2} + f_p(x_{1e})\Big|_{x_{1e}=c\alpha\bar{u}^+} < 0 \\ &= -\frac{\bar{u}^-}{k_2} + \frac{\bar{u}^+}{k_2} - \omega\alpha c\bar{u}^+ < 0. \end{aligned} \tag{72}$$

Using our parameterization of $\bar{u}^+$ and $\bar{u}^-$ from (10)-(11) and k_2 from (52), this becomes

$$\frac{2\lambda}{\sqrt{2\lambda-\lambda^2}} - (1-\gamma) < 0. \tag{73}$$

Performing a similar analysis for $x_{1e} = \alpha c\bar{u}^-$ and requiring that the *lower* boundary be *positive* at this point, we find that

$$|\gamma| < 1 - \frac{2\lambda}{\sqrt{2\lambda-\lambda^2}}, \tag{74}$$

which is Condition *CII*.

Now, we will show (ii). Along the segments CD and $\bar{D}\bar{C}$ we have $x_{2e} = \dot{x}_{1e} = 0$, so we must ensure that $\dot{x}_{2e} < 0$ for positive x_{1e} and $\dot{x}_{2e} > 0$ for negative x_{1e}. Consider the case for $x_{1e} > 0$. Because $x_{2e} = 0$ on CD, we have

$$\frac{\dot{x}_{2e}}{b_o} = -\frac{1}{c}x_{1e} + k_2 f_p(x_{1e}). \tag{75}$$

Observe also that along CD,

$$\frac{1}{b_o}\frac{\partial^2}{\partial x_{1e}^2}\dot{x}_{2e} = k_2 f_p''(x_{1e}). \tag{76}$$

We showed in Lemma 3 that $f_p''(x_{1e}) > 0$ if $x_\ell^+ \le x_{1e} \le 2\alpha c\bar{u}^+$. This implies any stationary point of (75) is a *minimum*, so that the maximum of (75) must occur at the boundary. Hence, it is sufficient to check that (75) is negative when $x_{1e} = 2\alpha c\bar{u}^+$ (it is clearly negative at point C because at point C, $f_p(x_{1e}) < 0$). Indeed, we find that

$$\begin{aligned} \frac{\dot{x}_{2e}}{b_o}\Big|_{x_{1e}=2\alpha c\bar{u}^+} &= -2\alpha\bar{u}^+ + \bar{u}^+ \\ &= \bar{u}^+(1-2\alpha) < 0 \text{ for } \alpha > 1/2 \end{aligned} \tag{77}$$

which holds since we have restricted $\alpha > 1/2$. ■

B. All Trajectories Enter $\mathcal{B}$ in Finite Time

We have shown that $\mathcal{P}$ is a globally attractive set and that $\mathcal{B}$ is an invariant set. We now show that $\mathcal{B}$ is also globally attractive by showing that all initial conditions which begin in $\mathcal{T}^\pm$ enter $\mathcal{B}$ in finite time.

Lemma 9: Suppose that Condition *CIII* holds and the conditions of Lemma 8 are satisfied. Then (i) the state exits $\mathcal{T}^\pm$ in finite time and (ii) all states which exit $\mathcal{T}^+$ (resp., $\mathcal{T}^-$)

along GD (resp., $\bar{D}\bar{G}$) enter $\mathcal{B}$ by the end of one additional switch.

Proof: To show (i), we consider $\mathcal{T}^+$. By assumption, the conditions of Lemma 8 are satisfied so (77) gives an upper, strictly negative bound on the acceleration, $\dot{x}_{2e}$, in $\mathcal{T}^+$. When $x_{2e} \neq 0$ but still in $\mathcal{T}^+$, the acceleration becomes *more* negative. Call this bound $-\mu_1 = b_o\bar{u}^+(1-2\alpha)$, $\mu_1 > 0$. Then for any $x_{2e}(0) \in \mathcal{T}^+$,

$$\begin{aligned} x_{2e}(t) - x_{2e}(0) &= \int_0^t \dot{x}_{2e}(\tau)d\tau \\ &\leq -\mu_1 t. \end{aligned}$$

It follows, that after finite time, the state exits $\mathcal{T}^+$, which proves (i). A similar argument holds for $\mathcal{T}^-$. When the state exits $\mathcal{T}^+$ (resp., $\mathcal{T}^-$), this only occurs when either the state enters $\mathcal{B}$ via CD (resp., $\bar{D}\bar{C}$) or the state exits via GD (resp., $\bar{D}\bar{G}$). Part (ii) of the theorem deals with the second scenario.

To show (ii), suppose the state exits $\mathcal{T}^+$ along GD so that it re-enters $\mathcal{U}^-$. Then the next switch occurs when the state crosses the x_{1e}-axis. We can calculate this point by solving (4) for the time, t_s, when $x_{2e} = 0$ and using this in the x_{1e} component of (4). This gives,

$$x_{1e}(t_s) = \sqrt{\left(\frac{x_{2e}^0}{\omega}\right)^2 + (x_{1e}^o - c\bar{u}^-)^2} + c\bar{u}^-. \tag{78}$$

To prevent a limit cycle[4], we require that by the end of the next switch (i.e., in π/ω more units of time), the state enters $\mathcal{B}$. Depending on our choices of α, λ, and γ, the state could enter $\mathcal{B}$ while x_{1e} is still positive, in which case our job is done. However, if this does not happen, then the system will be under the constant control input $\bar{u}_p(t) = \bar{u}^+$ for at least half a rotation. One implication of *CIII* is that the x_{1e} component of point $\bar{C}$ is less than $\alpha c\bar{u}^-$. Thus if

$$-x_{1e}(t_s) + 2c\bar{u}^+ > \alpha c\bar{u}^- \tag{79}$$

holds, then we are guaranteed that the state enters $\mathcal{B}$. The left-hand side is found by reflecting the point $x_{1e}(t_s)$ about the origin and decreasing its magnitude by $2c\bar{u}^+$. The worst case to consider is when the state exits $\mathcal{T}^+$ with $x_{1e}^o = 2\alpha c\bar{u}^+$, $x_{2e}^o = 2u^+/k_2$. Using these initial conditions with (78), it is straightforward to solve the inequality in (79) to give (54). Repeating a similar argument but starting at $x(0) = [2\alpha c\bar{u}^-, -2u^+/k_2]$ yields (55). ■

Remark: Simulation results seem to indicate that satisfying *CII* implies satisfaction of *CIII*, though this fact has so far eluded proof. We also point out that *CII* is essentially required by convenience. If the condition is not satisfied, then, for example, the lower boundary of $\mathcal{P}$ at $x_{1e} = \alpha c\bar{u}^-$ could sink below the x_{1e}-axis. If we allowed this, defining region $\mathcal{T}^-$ becomes problematic. Ideally, we would integrate backwards from point $\bar{D}$ until the trajectory crosses the lower boundary. All points in $\mathcal{P}$ and to the left of this curve would be $\mathcal{T}^-$ and points to the right would be $\mathcal{B}$. Unfortunately, the non-linear feedback makes solving such a trajectory in closed-form unfeasible. Thus, we are left with Condition *CII*, which, though overly restrictive, permits a workable definition of region $\mathcal{T}^-$ and $\mathcal{T}^+$.

C. $\mathcal{B}$ Is Asymptotically Stable In The Sense of Lyapunov

We have shown that all states will become trapped within $\mathcal{B}$. Now, we show that for $x_e \in \mathcal{B}$, x_e tends asymptotically to the origin. We do this by determining a Lyapunov function $V(x_e)$ for the Region $\mathcal{B}$. For further information on Lyapunov stability, the interested reader is referred to [31], [40], [41].

Theorem 3: The region $\mathcal{B}$ is asymptotically stable about the origin of the x_e phase plane.

Proof: Define:

$$\begin{aligned} V(x_e) &:= \frac{1}{2}x_{2e}^2 + \int_0^{x_{1e}} q(s)ds, \\ q(x_{1e}) &:= \omega^2 x_{1e} - b_o k_2 f_p(x_{1e}). \end{aligned} \tag{80}$$

Differentiating (80) yields

$$\dot{V}(x_e) = -\, b_o k_2 x_{2e}^2 \leq 0, \ \ \forall x_e \in \mathcal{B}. \tag{81}$$

Let $S = \{x \in \mathcal{B} | \dot{V}(x_e) = 0\}$. Because $\mathcal{B}$ is compact and invariant, it only remains to show that the largest invariant subset of S is the origin [31, Thrm. 4.4]. Suppose $x_e(t)$ belongs identically to some subset of S. Then $x_{2e}(t) \equiv 0$ which implies that

$$\dot{x}_{2e} \equiv 0 \equiv -\omega^2 x_{1e} + b_o k_2 f_p(x_{1e}) \tag{82}$$

which is just $-q(x_{1e})$. We now argue that $-q(x_{1e}) = 0$ only when $x_{1e} = 0$. For this, it sufficient to show that $q(x_{1e})$ only changes sign (crosses zero) when x_{1e} does. If $x_{1e} > 0$, then by construction $f_p(x_{1e}) < 0$ until x_{1e} is between the line segment defined by CD. For that region, $-q(x_{1e})/b_o$ is the same as (75) in Lemma 8 which we showed is strictly negative. A similar argument shows that, $-q(x_{1e}) > 0$ when $x_{1e} < 0$. Thus the largest invariant subset of S is the origin, which proves the theorem. ■

VI. DESIGN CONSIDERATIONS

When the system is in the linear region, $\mathcal{L}$, the transient response behaves according to

$$\dot{x}_e = \left(A - B\begin{bmatrix}k_1 & k_2\end{bmatrix}\right)x_e \tag{83}$$

which means the closed-loop damping $\hat{\zeta}$ and natural frequency $\hat{\omega}$ are

$$\hat{\omega} = \omega\sqrt{1 + \frac{1-\lambda}{\alpha\lambda}}, \quad \hat{\zeta} = \frac{1}{2}\sqrt{\frac{2-\lambda}{\alpha^2\lambda + \alpha(1-\lambda)}}. \tag{84}$$

Moreover, (*CII*) can be written as

$$\lambda < \frac{2(1-|\gamma|)^2}{(1-|\gamma|)^2 + 4}. \tag{85}$$

Bearing in mind that γ parameterizes the holdable setpoints, (85) says that the closer to the boundaries of $\mathcal{H}_{eq}$ we wish to visit, the smaller the linear region must be. A plot of the maximum allowable λ vs γ is shown in Fig. 8. Additionally, we have plotted the minimum increase in closed-loop

---

[4] We wish to eliminate the possibility that the state can, e.g., exit $\mathcal{T}^+$, then enter $\mathcal{T}^-$.

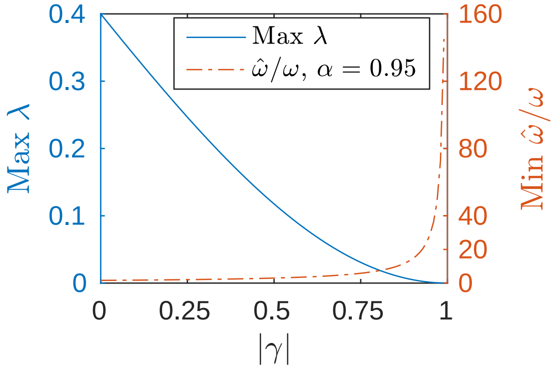

Fig. 8: The solid curve (left axis) plots the maximum allowable λ to satisfy *CII* for a given γ. The dash-dotted curve (right axis) plots the minimum increase in closed-loop bandwidth for a given γ such that *CII* is satisfied. The latter plot is for $\alpha = 0.95$, however, other values of α yield qualitatively similar results.

bandwidth vs $|\gamma|$ for $\alpha = 0.95$. For example, if we wish to visit setpoints, $x_{1r} \in (-0.8cu^+, 0.8cu^+)$, then we must have $\lambda < 0.02$ which, for $\alpha = 0.95$, implies that the closed-loop bandwidth has increased by approximately seven times. This has two immediate implications. First, if the control law is to be implemented digitally and we follow the rule of thumb that the sample frequency should be 30 times the closed-loop bandwidth [42], then the sample frequency would need to be about 210 times the system resonance. Second, the nearest mode that destroys our second-order assumption should be almost a decade away from the main second-order resonance. As we noted at the end of Section V-B, *CII* appears to be more restrictive than is strictly necessary for stability. Hence, if *CII* could be relaxed or replaced with a necessary and sufficient condition, these design considerations would be less limiting.

From (84), the closed-loop damping depends on λ and α. However, for a fixed λ, $\hat{\zeta}$ will increase as the discount factor α decreases. Moreover, if $\lambda << 1$, then $2 - \lambda \approx 2$, $1 - \lambda \approx 1$, and $\alpha^2\lambda \approx 0$ so $\hat{\zeta} \approx \frac{1}{\sqrt{2\alpha}}$. Thus, in general we expect the closed-loop response in the linear region to be well damped and that this damping increases with decreasing α.

VII. A METHOD FOR PRACTICAL IMPLEMENTATION

In this section we present a scaling method which allows the PTOSω or PTOS$\omega\zeta$ to be efficiently implemented in hardware. Both the PTOSω and PTOS$\omega\zeta$ require the evaluation of a complex function which cannot be accomplished with standard arithmetic operations: the square root in the case of PTOSω or the inversion of $x_1^*(t_k)$ associated with (18) in the case of PTOS$\omega\zeta$. In general, both functions will require some sort of iterative root finding method, e.g., Newton's method. Any iterative scheme has a negative affect on latency or hardware resources. A faster and more practical solution is to represent $\hat{f}_{to}$ (or $f_p(x_1)$) as a look-up table.

The key challenge in using a look-up table to represent $\hat{f}_{to}$ is that $\hat{f}_{to}$ changes for each new setpoint and it is impractical to store a different switching curve for every possible setpoint. Here, we show how this difficulty may be overcome by storing only the regulator curve and scaling the input and output.

Denote by $\hat{f}_{to}(x_1|0)$ the regulator switching curve and by $\hat{f}_{to}(x_{1e}|x_{1r})$ the setpoint tracking switching curve. Examination of (18) shows that the only difference between $\hat{f}_{to}(x_1|0)$ and $\hat{f}_{to}(x_{1e}|x_{1r})$ is the leading term, $\bar{u}^{\pm}$, which will be $\pm u^+$ in the regulator case. Hence, $\hat{f}_{to}(x_1|0)$ and $\hat{f}_{to}(x_{1e}|x_{1r})$ are related by

$$\hat{f}_{to}(x_{1e}|x_{1r}) = |\mathrm{sgn}_a(x_{1e})|\hat{f}_{to}\left(\frac{x_{1e}}{|\mathrm{sgn}_a(x_{1e})|}\middle|0\right). \qquad (86)$$

In other words, we can store *only* the regulator switching curve $\hat{f}_{to}(x_1|0)$ as a look-up table. Evaluation of any $\hat{f}_{to}(x_1|x_{1r})$ can be effected by scaling the input and output to $\hat{f}_{to}(x_1|0)$ according to (86). We demonstrate an implementation of this method on a Field Programmable Gate Array (FPGA) in the next section.

VIII. EXPERIMENTAL RESULTS

In this section we give a hardware demonstration of both the PTOSω and PTOS$\omega\zeta$ setpoint tracking control laws (50) in Sections VIII-A and VIII-B. In Section VIII-C, we provide a simulation comparison between the PTOSω to the high-gain near time-optimal control of [15].

Our original motivation for deriving PTOS$\omega(\zeta)$ was an AFM nano-positioning stage [26], [27]. Although some AFMs are well represented by a second-order model [8], the dynamics of the experimental stage in our lab are considerably more complex than a second-order system [43] and would require considerations beyond the framework presented here. To minimize such excursions, we instead use the LRC circuit shown in Fig. 9 as our plant, which is described by the transfer function

$$\frac{V_o(s)}{V_{in}(s)} = \frac{1/(LC)}{s^2 + \frac{R}{L}s + \frac{1}{LC}}. \qquad (87)$$

For both experiments, we programmed the control laws into a National Instruments Compact RIO (NI cRIO-9082) FPGA, using a sample frequency of $F_s = 100$ kHz. Because our control law utilizes both states of the system, we implemented a digital prediction observer on the FPGA to provide an estimate of the state, denoted $\hat{x} = [\hat{x}_1\ \hat{x}_2]^T$. For both cases, we chose λ as small as possible while keeping the closed-loop bandwidth in the linear region reasonably close to 100 kHz/30 $\approx$ 3.3 kHz. All plant and controller parameter values are summarized in Table I. The plant parameters are estimated via a white noise system identification routine, rather than computed from the nominal component values.

In both cases, we compare the experimental results to two simulations. First, we compare to a simulation of the PTOS$\omega(\zeta)$ controller implemented in continuous time with direct measurements of both states. To show the level of sub-optimality, we also show the ideal time-optimal solution. The experiments for both PTOSω and PTOS$\omega\zeta$ impose a saturation level of $u^+ = 1$ volt.

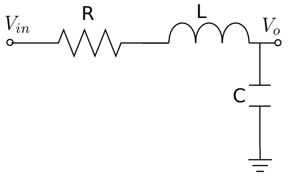

Fig. 9: Schematic of the RLC circuit used to test the control law.

A. No Damping PTOSω

If we could construct the circuit with $R = 0$, we would have exactly the plant described in (1) with $\zeta = 0$. Of course, this is impossible but we can get close. We chose a capacitor and inductor which have nominal values $C = 0.235\ \mu$F and $L = 100$ mH. The inductor has an internal resistance of $R = 82\ \Omega$. In constructing a passive circuit with extremely high Q, choosing a larger inductor tends to increase its internal resistance. Of course, we could try to increase $\omega = \sqrt{1/LC}$ by choosing smaller capacitance values and could thus theoretically get arbitrarily low damping. However, since the control law is implemented digitally on an FPGA, this approach is limited by the achievable sample rate. The values chosen represent a compromise between these competing concerns.

The system identification yields

$$G_1(s) = \frac{4.47806e7}{s^2 + 843.519s + 4.44851e7}. \tag{88}$$

Thus, $\zeta = 0.06$. We induced an initial condition by issuing a step command of $V_{in} = 1$ volt to the system. After a settling period, we turned on the PTOSω controller with a reference value of $x_{1r} = -0.5cu^+$. We set $\lambda = 0.1$ and $\alpha = 0.85$. In the linear region, this gives a closed-loop bandwidth of approximately 3.61 kHz which is about 27.7 times less than the sample rate. Since our control law was designed for continuous time, this represents essentially the lower bound on λ given the sample rate.

The results of this experiment are displayed in Figs. 10 and 11, where the results of the two simulations are also plotted. First, we simulate with the PTOSω controller designed as though the plant has zero damping, but with the simulation plant as (88) and with both states directly available. For comparison, we also simulate the time-optimal controller.

B. PTOS$\omega\zeta$

In implementing the PTOS$\omega\zeta$, we employed the method developed in Section VII to evaluate f_p. We added a 1 kΩ resistor in series with the inductor. The system identification yields

$$G_2(s) = \frac{4.07385e7}{s^2 + 9844.84s + 4.0891e7} \tag{89}$$

which has a damping of $\zeta = 0.77$. As outlined in Section VII, we generated the regulator $\hat{f}_{to}(x_1|0)$ as a look-up table. To ease implementation details, we defined an evenly spaced grid of 1024 points for x_1 in the interval $(-2cu^+, 2cu^+)$. We then computed $\hat{f}_{to}(x_1|0)$ at these grid points offline. This data is stored in the memory of the FPGA and a routine was programmed to perform linear interpolation between the

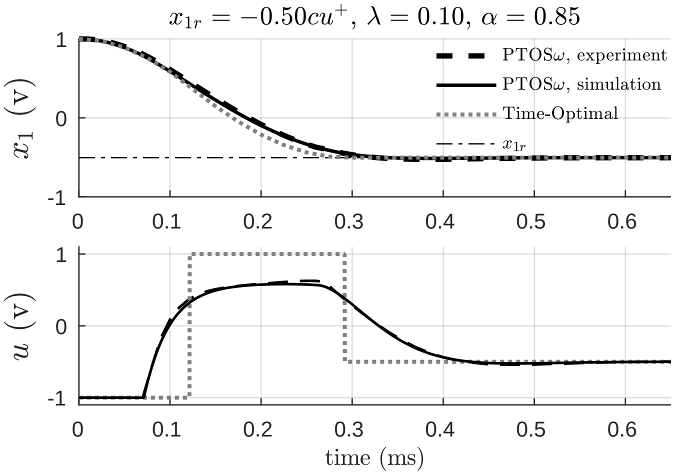

Fig. 10: Comparison between simulation and experimental results for the reference tracking PTOSω for the system G_1. The initial condition is set to $x_1 = 1 \cdot c$ and the reference is $x_{1r} = -0.5cu^+$.

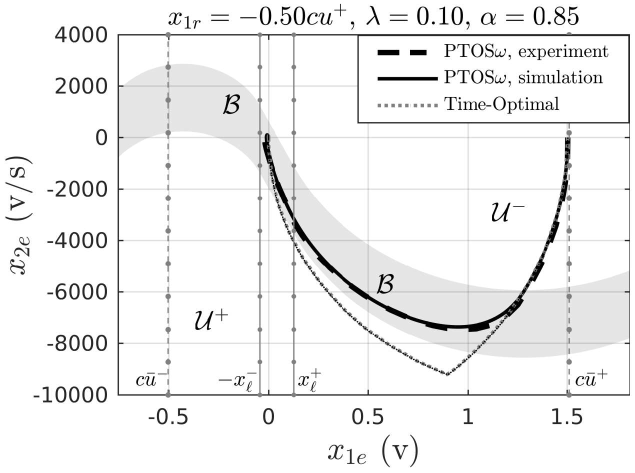

Fig. 11: Phase-plane trajectories in the error coordinates of both the simulated and experimental systems for the system G_1.

TABLE I: Summary of plant and controller parameters. In the last table, t_s is the settle time in seconds for the Time-Optimal simulation (opt.), the PTOS$\omega(\zeta)$ simulation (sim.), and the PTOS$\omega(\zeta)$ experiment (exp.).

System	Plant Parameters					
	ω (rad/s)	ζ	b_o	R (Ω)	L (mH)	C (μF)
G_1	6.67e3	0.06	4.48e7	82	100	0.235
G_2	6.39e3	0.77	4.07e7	1082	100	0.235

	Controller Parameters			
	α	λ	$K = \begin{bmatrix} k_1 & k_2 \end{bmatrix}$	Observer gain
G_1	0.85	0.1	[10.5, 7.64e-4]	$\begin{bmatrix} 0.337 & 2532 \end{bmatrix}^T$
G_2	0.85	0.15	[11.8, 6.65e-4]	$\begin{bmatrix} 0.387 & 2358 \end{bmatrix}^T$

	Closed-Loop Characteristics				
	F_{bw} (kHz)	$\hat{\zeta}$	t_s(opt.)	t_s(sim.)	t_s(exp.)
G_1	3.61	0.772	2.82e-4	4.53e-4	5.10e-4
G_2	3.63	0.81	3.57e-4	4.89e-4	5.50e-4

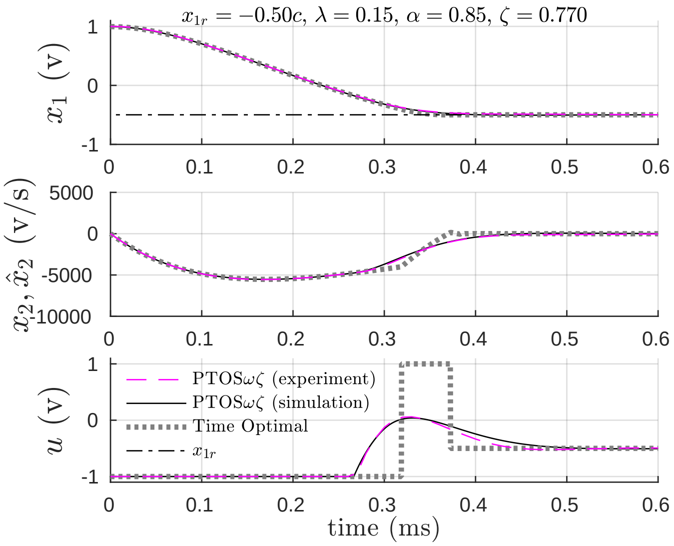

Fig. 12: Time history of the PTOS$\omega\zeta$ controller and a plant with a damping factor of $\zeta = 0.77$.

grid points. Here, we use $\alpha = 0.85$ and $\lambda = 0.15$ which gives a closed-loop bandwidth of 3.63 kHz. For this experiment, we use the same initial conditions and setpoint as in Section VIII-A. The results of this experiment are plotted in Fig. 12 along with the simulated PTOS$\omega\zeta$ and time-optimal responses.

C. Comparison to High-Gain Feedback

In [15], the authors develop a remarkably simple feedback law to approximate time-optimal control. To our knowledge, their method is the only practical approximation to time-optimal feedback control applicable to (1) when $\zeta = 0$. Their method centers around the observation that if the initial state is within a single switch from the origin (e.g, $x_o \in \mathcal{Q}$ in our case), then the non-linear time-optimal switching curve can be replaced with a linear switching plane. This plane is constructed such that it connects the origin of the error phase-plane with the point of the last switch on the time-optimal switching curve. The time-optimal version of the control law is given by

$$\bar{u}(t) = \mathrm{sgn}_a(-s)$$
$$s = x_{2e} + \rho x_{1e}$$

where ρ defines the slope of the linear switching plane and depends on the initial condition, x_o. To avoid chattering, they introduce a finite gain and a saturator such that one implements

$$\bar{u}(t) = \mathrm{sat}_a(-k(\rho x_{1e} + x_{2e})).$$

Fig. 13 compares the normalized responses of the PTOSω with this control law using the same plant and PTOSω parameters as Section VIII-A. Each trajectory has the same initial condition of $x_o = [-0.5cu^+, 0]^T$ while the setpoints are $-0.3cu^+$, $0.1cu^+$ and $0.6cu^+$. The only tuning parameter for the high-gain linear controller is k, which we choose to yield the same closed-loop bandwidth as the PTOSω control law in the unsaturated region.

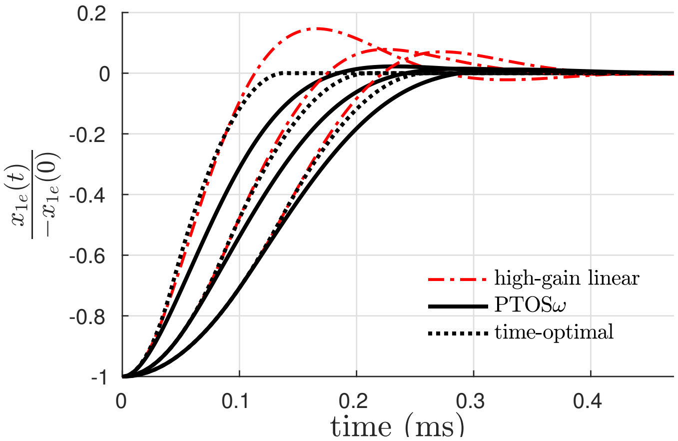

Fig. 13: Comparison of normalized responses between time-optimal control (dotted), PTOSω (solid) and high-gain linear feedback (dash-dotted) for setpoints (left to right) $-0.3cu^+$, $0.1cu^+$ and $0.6cu^+$ and initial condition $x_o = [-0.5cu^+, 0]^T$.

D. Discussion

For the listed control parameters, the experiments of Section VIII-A and VIII-B performed quite well and match with the simulated results nicely. In theory, decreasing λ below the values used here should yield even faster responses that approach the time-optimal response. However, in other trials not shown, this resulted in a deterioration in performance, likely due to the discretization of the control law. Although the simulated time-optimal results are significantly faster, these results represent a theoretical lower bound on the settle time which are not achievable in practice. As noted in Section II-B, this is due to a combination of finite actuation bandwidth and delay, model uncertainty and process noise.

The comparison in Section VIII-C shows that the PTOSω performs competitively. While the rise-time of the high-gain controller is generally better than the PTOSω, the high-gain method in general exhibits significantly more overshoot which negatively affects the settling times. While the overshoot can be mitigated by increasing k, this will result in a very high closed-loop bandwidth which may not be achievable in practice and also implies that one should decrease λ in the PTOSω controller to give a fair comparison. The clear advantage of the high-gain method is that it can be applied to n-th order plants and is simple to implement (though as [15] mentions, one must either compute ρ and k online or provide a look-up table for interpolation). On the other hand, the PTOSω appears to provide better damping and more consistent performance across movement ranges.

IX. CONCLUSIONS AND FUTURE WORK

In this paper, we reviewed the derivation of the time-optimal setpoint tracking controller for the harmonic oscillator, which we noted can be viewed as a time-optimal regulator with asymmetric saturation limits in the error coordinates. Using this development, we derived the PTOSω and PTOS$\omega\zeta$ setpoint tracking controllers, which have finite bandwidth and smoothly blend a non-linear controller into a standard linear feedback law. We then proved stability of the PTOSω provided certain conditions are satisfied. Moreover, we showed how either method can be efficiently implemented using a *single* look-up table combined with a simple scaling method. Finally, we demonstrated that both controllers perform well in practice.

Future work should investigate proving stability for the case with damping. Our stability proof for the un-damped case relied heavily on having an explicit, closed-form expression for f_p as well as k_1 and k_2. Since similar expressions do not exist when damping is included, a stability proof will require a different strategy. For example, a possible method to derive an invariant region analogous to $\mathcal{B}$ might consider the angle between the vector field along the boundary of $\mathcal{B}$ and boundary itself. However, the tails $\mathcal{T}^{\pm}$ will still exist and deriving a condition to guarantee that when the state exits $\mathcal{T}^{+}$ or $\mathcal{T}^{-}$ it must enter the invariant region (as in Section V-B) in finite time will be challenging.

Future research should also investigate digital implementation issues by determining the slowest sample rate for which stability can be guaranteed or by developing a fully discretized version. Replacing the sufficient conditions for stability, *CII* and *CIII*, with sufficient and necessary conditions should result in an increased range of permissible λ and γ. Due to the increased complexity over using the rigid-body switching curve as in [2], [3], further investigation could consider how much optimality is gained through our approach and for which parameter values their method fails.

REFERENCES

[1] M. Ordonez, M. T. Iqbal, and J. E. Quaicoe, “Selection of a curved switching surface for buck converters,” *IEEE Trans. Power Electronics*, vol. 21, no. 4, pp. 1148–1153, July 2006.

[2] J. Y. Jeong, C. W. Lee, C. C. Chung, and Y. S. Kim, “A discrete-time modified sliding mode proximate time-optimal servomechanism for scanning-probe-microscope-based data storage,” *IEEE Trans. Magnetics*, vol. 44, no. 11, pp. 3750–3753, Nov. 2008.

[3] A. Sebastian, A. Pantazi, G. Cherubini, M. Lantz, H. Rothuizen, H. Pozidis, and E. Eleftheriou, “Towards faster data access: Seek operations in MEMS-based storage devices,” in *Proc. IEEE Conf. Control Applications*, Oct. 2006, pp. 283–288.

[4] A. Pantazi, M. A. Lantz, G. Cherubini, H. Pozidis, and E. Eleftheriou, “A servomechanism for a micro-electro-mechanical-system-based scanning-probe data storage device,” *Nanotechnology*, vol. 15, no. 10, p. S612, 2004.

[5] J. Seitz, “Time-optimal control and switching surface of the swing equation,” Master’s thesis, Swiss Federal Inst. of Tech., Zurich, Switzerland, Jan. 2017.

[6] S. Andersson and L. Pao, “Non-raster sampling in atomic force microscopy: A compressed sensing approach,” in *Proc. American Control Conf.*, June 2012, pp. 2485–2490.

[7] P. Huang and S. B. Andersson, “Fast scanning in AFM using non-raster sampling and time-optimal trajectories,” in *Proc. IEEE Conf. Decision and Control*, Dec. 2012, pp. 5073–5078.

[8] A. J. Fleming and K. K. Leang, *Design, Modeling and Control of Nanopositioning Systems*. London: Springer, 2014.

[9] A. Bryson and Y. Ho, *Applied Optimal Control*. New York: Hemisphere Pub. Corp., 1975.

[10] E. P. Ryan, *Optimal Relay and Saturating Control System Synthesis*. New York: Peter Peregrinus, 1982.

[11] R. Oldenburger and G. Thompson, “Introduction to time optimal control of stationary linear systems,” *Automatica*, vol. 1, no. 23, pp. 177 – 205, 1963.

[12] M. Athans and P. L. Falb, *Optimal Control*. New York: McGraw-Hill, 1966.

[13] E. Ryan, “On the sensitivity of a time-optimal switching function,” *IEEE Trans. Automatic Control*, vol. 25, no. 2, pp. 275–277, Apr. 1980.

[14] J. L. Junkins and Y. Kim, *Introduction to Dynamics and Control of Flexible Structures*. Washington, DC: American Institute of Aeronautics and Astronautics, Inc., 1993.

[15] S.-T. Wu, “Time-optimal control and high-gain linear state feedback,” *Int. J. Control*, vol. 72, no. 9, pp. 764–772, 1999.

[16] M. Workman, “Adaptive proximate time-optimal servomechanisms,” Ph.D. dissertation, Stanford University, Stanford, CA, Mar. 1987.

[17] M. L. Workman, R. L. Kosut, and G. F. Franklin, “Adaptive proximate time-optimal servomechanisms: Continuous time case,” in *Proc. American Control Conf.*, June 1987, pp. 589–594.

[18] M. L. Workman and G. F. Franklin, “Implementation of adaptive proximate time-optimal controllers,” in *Proc. American Control Conf.*, June 1988, pp. 1629–1635.

[19] L. Pao and G. Franklin, “Proximate time-optimal control of third-order servomechanisms,” *IEEE Trans. Automatic Control*, vol. 38, no. 4, pp. 560–580, Apr. 1993.

[20] Y.-M. Choi, J. Jeong, and D.-G. Gweon, “A novel damping scheduling scheme for proximate time optimal servomechanisms in hard disk drives,” *IEEE Trans. Magnetics*, vol. 42, no. 3, pp. 468–472, Mar. 2006.

[21] A. T. Salton, Z. Chen, and M. Fu, “Improved servomechanism control design-nonswitching case,” *IFAC Proceedings Volumes*, vol. 44, no. 1, pp. 8614 – 8619, 2011.

[22] ——, “Improved control design methods for proximate time-optimal servomechanisms,” *IEEE/ASME Trans. Mechatronics*, vol. 17, no. 6, pp. 1049–1058, Dec. 2012.

[23] T. Lu and G. Cheng, “Expanded proximate time-optimal servo control for motor position regulation,” in *Proc. Chinese Control and Decision Conf.*, May 2015, pp. 5387–5392.

[24] A. Pascoal, R. Kosut, G. Franklin, D. Meldrum, and M. Workman, “Adaptive time-optimal control of flexible structures,” in *Proc. American Control Conf.*, June 1989, pp. 19–24.

[25] A. Dhanda and G. F. Franklin, “An improved 2-DOF proximate time optimal servomechanism,” *IEEE Trans. Magnetics*, vol. 45, no. 5, pp. 2151–2164, May 2009.

[26] R. A. Braker and L. Y. Pao, “Proximate time-optimal control of a second-order flexible structure,” in *Proc. IEEE Conf. Control Applications*, Sep. 2015, pp. 840–845.

[27] ——, “Proximate time-optimal reference tracking of an undamped harmonic oscillator,” in *Proc. American Control Conf.*, July 2016, pp. 6221–6226.

[28] Z. Shen, P. Huang, and S. B. Andersson, “Calculating switching times for the time-optimal control of single-input, single-output second-order systems,” *Automatica*, vol. 49, no. 5, pp. 1340 – 1347, 2013.

[29] H. Knudsen, “Maximum effort control for an oscillatory element,” Ph.D. dissertation, University of California, Berkeley, Berkeley, CA, 1960.

[30] D. E. Kirk, *Optimal Control Theory - An Introduction*. Dover Publications, 1998.

[31] H. K. Khalil, *Nonlinear Systems*, 3rd ed. Upper Saddle River, NJ: Prentice Hall, 1996.

[32] J.-J. Slotine and W. Li, *Applied Nonlinear Control*. Englewood Cliffs, New Jersey: Prentice Hall, 1991.

[33] lyas Eker, “Second-order sliding mode control with experimental application,” *ISA Trans.*, vol. 49, no. 3, pp. 394–405, July 2010.

[34] J.-L. Chang, “On chattering-free dynamic sliding mode controller design,” *J. Control Science and Eng.*, vol. 2012, no. Article ID 564906, p. 7, 2012.

[35] A. Ferrara and M. Rubagotti, “A sub-optimal second order sliding mode controller for systems with saturating actuators,” *IEEE Trans. Automatic Control*, vol. 54, no. 5, pp. 1082–1087, May 2009.

[36] S. Mondal and C. Mahanta, “Nonlinear sliding surface based second order sliding mode controller for uncertain linear systems,” *Communications in Nonlinear Science and Numerical Simulation*, vol. 16, no. 9, pp. 3760 – 3769, 2011.

[37] B. Bandyopadhyay and D. Fulwani, “High-performance tracking controller for discrete plant using nonlinear sliding surface,” *IEEE Trans. Industrial Electronics*, vol. 56, no. 9, pp. 3628–3637, Sep. 2009.

[38] B. B. S. Janardhanan and S. K. Spurgeon, *Advances in Sliding Mode Control: Concept, Theory and Implementation*. New York: Springer, 2013.

[39] S. Weerasooriya, T. S. Low, and Y. H. Huang, “Adaptive time optimal control of a disk drive actuator,” *IEEE Trans. Magnetics*, vol. 30, no. 6, pp. 4224–4226, Nov. 1994.

[40] J. LaSalle and S. Lefschetz, *Stability by Liapunov’s Direct Method With Applications*. New York: Academic Press, 1961.

[41] R. E. Kalman and J. E. Bertram, “Control system analysis and design via the ’Second Method’ of Lyapunov: I continuous-time systems,” *ASME J. Basic Eng.*, vol. 82, no. 2, pp. 371–393, June 1960.

[42] G. F. Franklin, J. D. Powell, and M. Workman, *Digital Control of Dynamic Systems*. Half Moon Bay, CA: Ellis-Kagle Press, 1998.

[43] R. A. Braker and L. Y. Pao, "Fast setpoint tracking of an atomic force microscope x-y stage via optimal trajectory tracking," in *Proc. American Control Conf.*, May 2017, pp. 2875–2881.

Roger A. Braker earned the B.A. degree in physics from the University of Oklahoma in 2005 and the M.S. degree in electrical engineering from the University of Colorado in 2017.

Since 2014, he has been a graduate student in the Electrical, Computer, and Energy Engineering Department at the University of Colorado Boulder. His research focuses on the application of optimal control methods to Atomic Force Microscopy.

Lucy Y. Pao earned B.S., M.S., and Ph.D. degrees in electrical engineering from Stanford University.

She is currently a Professor in the Electrical, Computer, and Energy Engineering Department and a Professor (by courtesy) in the Aerospace Engineering Sciences Department at the University of Colorado Boulder. Her research has primarily been in the control systems area, with applications ranging from atomic force microscopy to disk drives to digital tape drives to megawatt wind turbines and wind farms.

Dr. Pao received a National Science Foundation (NSF) Early Faculty CAREER Award, an Office of Naval Research (ONR) Young Investigator Award, and an International Federation of Automatic Control (IFAC) World Congress Young Author Prize. Selected recent honors include elevation to IEEE Fellow in 2012, the 2012 IEEE Control Systems Magazine Outstanding Paper Award (with K. Johnson), election to Fellow of IFAC in 2013, and the 2015 SIAM J. Control and Optimization Best Paper Prize (with J. Marden and H. P. Young). Selected recent and current professional society activities include being General Chair for the 2013 American Control Conference, an IEEE Control Systems Society (CSS) Distinguished Lecturer (2008-2014), a member of the IEEE CSS Board of Governors (2011- 2013 (elected) and 2015 (appointed)), Fellow of the Renewable and Sustainable Energy Institute (2009-present), IEEE CSS Fellow Nominations Chair (2016-), member of the IFAC Fellow Selection Committee (2014-2017), and member of the International Program Committees for the 2016 Indian Control Conference, the 2016 IFAC Symposium on Mechatronic Systems, and the 2017 IFAC World Congress. Most recently, she received the 2017 Control Engineering Practice award from the American Automatic Control Council and the 2017 European Academy of Wind Energy Scientific Award.